Cell Reports

Article

Autocrine activation of MAPK signaling mediates intrinsic tolerance to androgen deprivation in LY6D prostate cancer cells

Graphical abstract

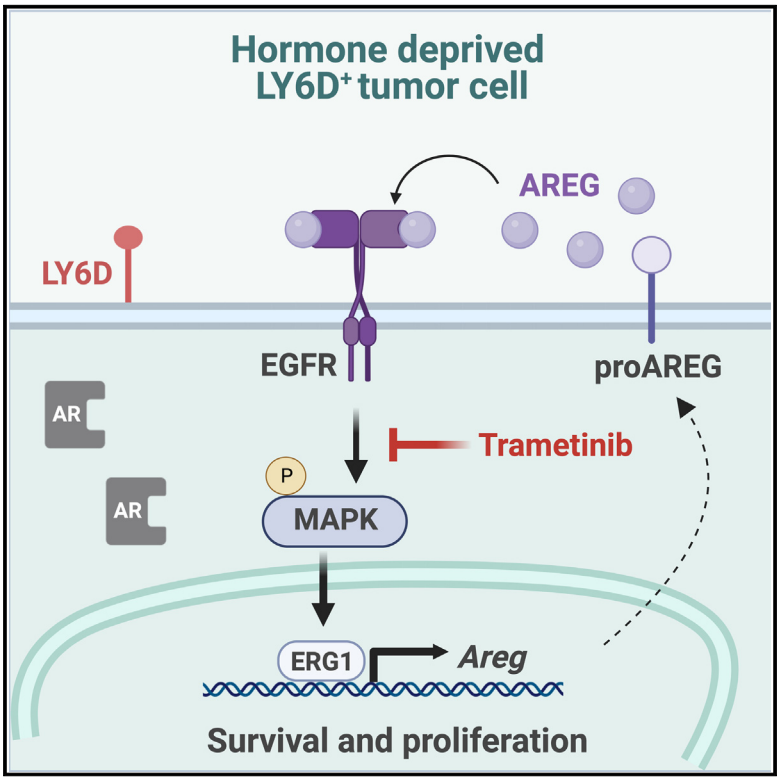

Authors

Ivana Steiner,
Teresita del N.J. Flores-Tellez,
Renaud Mevel, ..., Ananya Choudhury,
Georges Lacaud, Esther Baena

Correspondence

esther.baena@cruk.manchester.ac.uk

In brief

Steiner et al. demonstrate that PTEN deletion in luminal prostate cell causes an expansion of transformed LY6D$^+$ progenitor cells with intrinsic castration-resistant properties through autocrine AREG-mediated MAPK activation. Pharmacological interference of MAPK pathway overcomes the castration-resistance properties of LY6D$^+$ cells, providing a rationale to target pre-existent castration-resistant cells at early stages.

Highlights

- Luminal-restrictive PTEN deletion causes expansion of LY6D$^+$ prostate progenitors
- AREG-mediated MAPK activation drives castration resistance in LY6D$^+$ cells
- LY6D$^+$ tumor cells are enriched in high-grade and androgen-resistant prostate cancer
- MAPK inhibition overcomes the inherent resistance properties of LY6D$^+$ cells

Steiner et al., 2023, Cell Reports *42*, 112377
April 25, 2023
https://doi.org/10.1016/j.celrep.2023.112377

CellPress

Cell Reports

CellPress
OPEN ACCESS

Article

Autocrine activation of MAPK signaling mediates intrinsic tolerance to androgen deprivation in LY6D prostate cancer cells

Ivana Steiner,[1,12] Teresita del N.J. Flores-Tellez,[1,12] Renaud Mevel,[2] Amin Ali,[1,9] Pengbo Wang,[1] Pieta Schofield,[3] Caron Behan,[3] Nicholas Forsythe,[4,9] Garry Ashton,[3] Catherine Taylor,[5] Ian G. Mills,[4,9,10,11] Pedro Oliveira,[6] Simon S. McDade,[4,9] Dietmar M. Zaiss,[7] Ananya Choudhury,[5,8,9] Georges Lacaud,[2] and Esther Baena[1,9,13,*]

[1]Prostate Oncobiology Group, Cancer Research UK Manchester Institute, The University of Manchester, Alderley Park, SK10 4TG Macclesfield, UK

[2]Stem Cell Biology Group, Cancer Research UK Manchester Institute, The University of Manchester, Alderley Park, SK10 4TG Macclesfield, UK

[3]Cancer Research UK Manchester Institute, The University of Manchester, Alderley Park, SK10 4TG Macclesfield, UK

[4]Patrick G Johnston Centre for Cancer Research, Queen's University Belfast, Belfast, BT9 7BL Northern Ireland, UK

[5]The Christie NHS Foundation Trust, Manchester Academic Health Sciences Centre, M20 4BX Manchester, UK

[6]Department of Pathology, The Christie NHS Foundation Trust, M20 4BX Manchester, UK

[7]Department of Immune Medicine, University Regensburg, Institute of Clinical Chemistry and Laboratory Medicine, University Hospital Regensburg, and Leibniz Institute for Immunotherapy (LIT), 93053 Regensburg, Germany

[8]The University of Manchester, Manchester Cancer Research Centre, M20 4BX Manchester, UK

[9]Belfast-Manchester Movember Centre of Excellence, Cancer Research UK Manchester Institute, The University of Manchester, Alderley Park, SK10 4TG Macclesfield, UK

[10]Nuffield Department of Surgical Sciences, John Radcliffe Hospital, University of Oxford, OX3 9DU Oxford, UK

[11]Department of Clinical Sciences and Centre for Cancer Biomarkers, University of Bergen, 7804 Bergen, Norway

[12]These authors contributed equally

[13]Lead contact

*Correspondence: esther.baena@cruk.manchester.ac.uk

https://doi.org/10.1016/j.celrep.2023.112377

SUMMARY

The emergence of castration-resistant prostate cancer remains an area of unmet clinical need. We recently identified a subpopulation of normal prostate progenitor cells, characterized by an intrinsic resistance to androgen deprivation and expression of LY6D. We here demonstrate that conditional deletion of PTEN in the murine prostate epithelium causes an expansion of transformed LY6D$^+$ progenitor cells without impairing stem cell properties. Transcriptomic analyses of LY6D$^+$ luminal cells identified an autocrine positive feedback loop, based on the secretion of amphiregulin (AREG)-mediated activation of mitogen-activated protein kinase (MAPK) signaling, increasing cellular fitness and organoid formation. Pharmacological interference with this pathway overcomes the castration-resistant properties of LY6D$^+$ cells with a suppression of organoid formation and loss of LY6D$^+$ cells *in vivo*. Notably, LY6D$^+$ tumor cells are enriched in high-grade and androgen-resistant prostate cancer, providing clinical evidence for their contribution to advanced disease. Our data indicate that early interference with MAPK inhibitors can prevent progression of castration-resistant prostate cancer.

INTRODUCTION

Primary prostate cancer (PCa) comprises a spectrum of clinically, morphologically, and molecularly heterogeneous disease phenotypes, which frequently include multiple tumor foci within the same patient, with diverse genomic and molecular profiles.[1–4] Genetic lineage-tracing studies, organoid models, and single-cell profiling have been instrumental in interrogating the cellular heterogeneity of the basal and luminal prostate compartments.[5–14] Within given tumor foci, individual cells and distinct cell lineages differ in their capacity for oncogenic transformation and tumor initiation. Notably, the contribution of diverse cellular subtypes to human PCa is still poorly defined. Recent single-cell studies have dissected the cellular anatomy of the mouse and human prostate, both in hormonally naive and hormone-treated normal prostate.[6,8,9,11,12,15,16] These studies confirmed the considerable complexity of cellular subtypes within the prostatic epithelial compartment. Notably, while the basal lineage was relatively homogeneous, the luminal lineage showed high cellular heterogeneity with multiple cell subtypes, including secretory luminal, stem-like luminal, and periurethral luminal cells.[6,8,9,11,12,16]

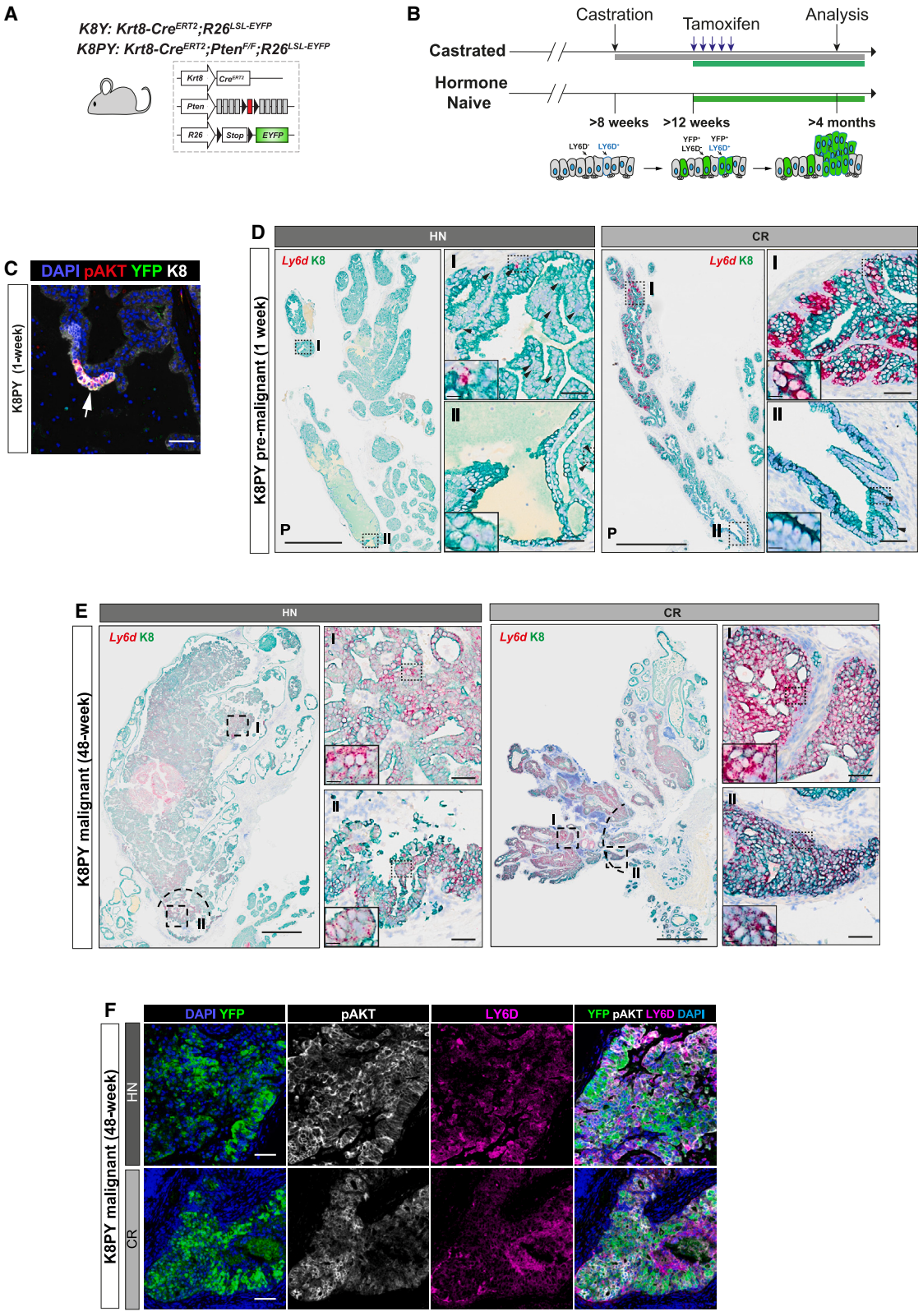

(legend on next page)

The development of PCa is strongly associated with loss of PTEN function,[17,18] which frequency increases in metastatic PCa.[19–21] PTEN is a critical regulator of key cellular processes in normal and malignant epithelial cells as well as in immune cells and thereby also orchestrates tumor microenvironment responses.[22,23] Numerous studies have demonstrated that both basal and luminal PTEN-deficient cells can be the cell of origin for PCa, albeit with different tumor-initiating latency.[7,14,24–26] These differential contributions of basal and luminal cells to prostate tumor dynamics illustrate the key role of the cell of origin and their unique cell-intrinsic properties to disease progression and potentially also to response to therapies.

We have previously identified LY6D as a cell-surface protein that marks intrinsically castration-resistant (CR) luminal prostate progenitors.[6] In organoid culture, untransformed LY6D$^+$ prostate cells exhibit higher organoid-forming potential compared with LY6D$^-$ cells, revealing their intrinsic stem and progenitor properties. Building upon these findings, we now define the underlying cell-intrinsic mechanism regulating CR prostate tumors initiated from LY6D$^+$ luminal progenitors. We identify that the intrinsic transcriptional regulatory program of LY6D$^+$ progenitor cells is required for survival of aggressive, treatment-resistant clones, based on an autocrine signaling pathway in CR LY6D$^+$ luminal cells, which involves amphiregulin (AREG) secretion and epidermal growth factor receptor (EGFR) signaling.

RESULTS

LY6D$^+$ luminal progenitor cells contribute to malignant transformation of PTEN-deficient tumors

We previously demonstrated that LY6D$^+$ luminal prostate progenitor cells are intrinsically resistant to androgen deprivation in non-tumor-prone mice.[6] To investigate whether LY6D$^+$ luminal cells also play a significant role for CR PCa, we employed a conditional mouse model, allowing for tumor initiation at any given time by systemic administration of tamoxifen. For this, we used an inducible luminal lineage-specific mouse model, where *Pten* deletion is induced in Keratin8 (K8$^+$) luminal cells (*K8-Cre^{ERT2}*; *Pten$^{Flox/Flox}$*;*Rosa26-Stop$^{Flox/Flox}$-EYFP*, hereafter *K8PY* mice), as well as age-matched *Pten*-competent mice as controls (*K8-Cre^{ERT2}*;*Rosa26-Stop$^{Flox/Flox}$-EYFP*; hereafter *K8Y* mice) (Figure 1A). Upon tamoxifen treatment (Figure 1B), activated CRE recombinase drives *Pten* deletion and expression of the enhanced yellow fluorescence protein (YFP) in K8$^+$ luminal cells (Figure 1C).

To assess the distribution of LY6D$^+$ progenitor cells in adult male mice across the entire organ prior to tumor initiation (1 week post tamoxifen treatment), whole prostates from hormone-naive (HN) and castrated (CR) mice were analyzed for the expression of *Ly6D* mRNA by RNA *in situ* hybridization (ISH) in the K8$^+$ luminal compartment in 12-week-old males. In keeping with our previous observations, LY6D$^+$ luminal progenitors are located in both proximal and luminal regions (Figure 1D). In contrast to young males (4 weeks old),[6] adult males showed a higher proportion of LY6D$^+$ progenitors in distal prostate regions in all lobes, irrespective of whether mice were castrated (CR) or not (HN). Importantly, the frequency of LY6D$^+$ cells was significantly higher in CR mice compared with HN males (Figures 1D, S1A, and S1B).

K8-driven loss of *Pten* triggers formation of low-grade prostate intraepithelial neoplasia (PIN) lesions in all prostate lobes 1 month post tamoxifen treatment.[7] These lesions then progress to high-grade PIN lesions (HG-PIN) 8–16 weeks after tamoxifen-induced recombination, which transform into early prostate adenocarcinoma at 24 weeks. We then evaluated the distribution of LY6D$^+$ progenitor cells 48 weeks after *Pten* deletion once high-grade PIN lesions have developed. In agreement with previous observations,[6] *Pten* deletion in CR luminal cells led to the development of high-grade PIN lesions and adenocarcinoma with cribriform morphology at earlier time points (Figure S1C). Our analyses indicated that the proportion of YFP$^+$LY6D$^+$ luminal tumor cells increased in PTEN-dependent tumors initiated from both HN and CR prostate luminal cells (Figures 1E and S1D–S1F). We further validated our findings from RNA-ISH staining by immunofluorescence (IF) (Figure S1G). In keeping with our RNA-ISH data, LY6D$^+$ cells were readily detectable in PTEN-deficient cells, identified by positive staining for YFP and phosphorylated alpha serine/threonine protein kinase (pAKT) in HN and CR prostates (Figure 1F).

In conclusion, our data indicate that LY6D$^+$ luminal cells are present in premalignant lesions and their frequency increases with PTEN-mediated tumor formation.

Organoid-forming capacity and castration resistance of LY6D$^+$ progenitor cells are not affected by PTEN loss

Besides their intrinsically CR properties, LY6D$^+$ cells are characterized by increased organoid-forming capacity.[6] *PTEN* loss has previously been reported to modulate epithelial growth and differentiation of prostate and mammary cells in organoid culture.[5,27,28] We therefore hypothesized that PTEN deletion in the prostate luminal compartment could affect the stem properties and organoid-forming capacity of LY6D$^+$ cells. To address this question, we assessed the frequency of luminal progenitor-like cells by isolating YFP$^+$LY6D$^+$ and YFP$^+$LY6D$^-$ prostate cells from K8Y control and K8PY PTEN-deficient mice (Figures 2A, 2B, and S2A–S2C). *Pten* deletion in the HN status resulted in a

Figure 1. Distribution of LY6D$^+$ luminal progenitor cells in PTEN-deficient prostate tumors

(A) Lineage-tracing strategy used for targeting luminal keratin 8 (K8)-expressing cells in K8Y and K8PY mice. Black triangles, *loxP* sites.

(B) Experimental approach. Mice (>8 weeks) were used in castrated (CR) and HN treatment groups.

(C) IF of murine prostate 1 week post tamoxifen treatment. K8 (white), lineage tracer YFP (green), and pAKT (red). Nuclei, DAPI. Scale bar, 50 μm.

(D) Immunohistochemical images of HN and CR premalignant K8PY prostates (1 week post tamoxifen). *Ly6d* by RNA-ISH (red) in the K8$^+$ cells (green). Representative images of K8PY murine prostates are shown. Left, scale bar, 1 mm. Right, distal (l) and proximal (ll) regions; scale bars, 50 and 10 μm, respectively.

(E) RNA-ISH *Ly6d* expression in HN and CR PTEN-deficient tumors (K8PY mice) 48 weeks post tamoxifen. Scale bars, 50 and 10 μm.

(F) IF of LY6D$^+$ cells in the YFP$^+$ pAKT$^+$ tumors in (E). YFP (green), pAKT (white), LY6D (magenta), DAPI (blue). Scale bar, 50 μm. See also Figure S1.

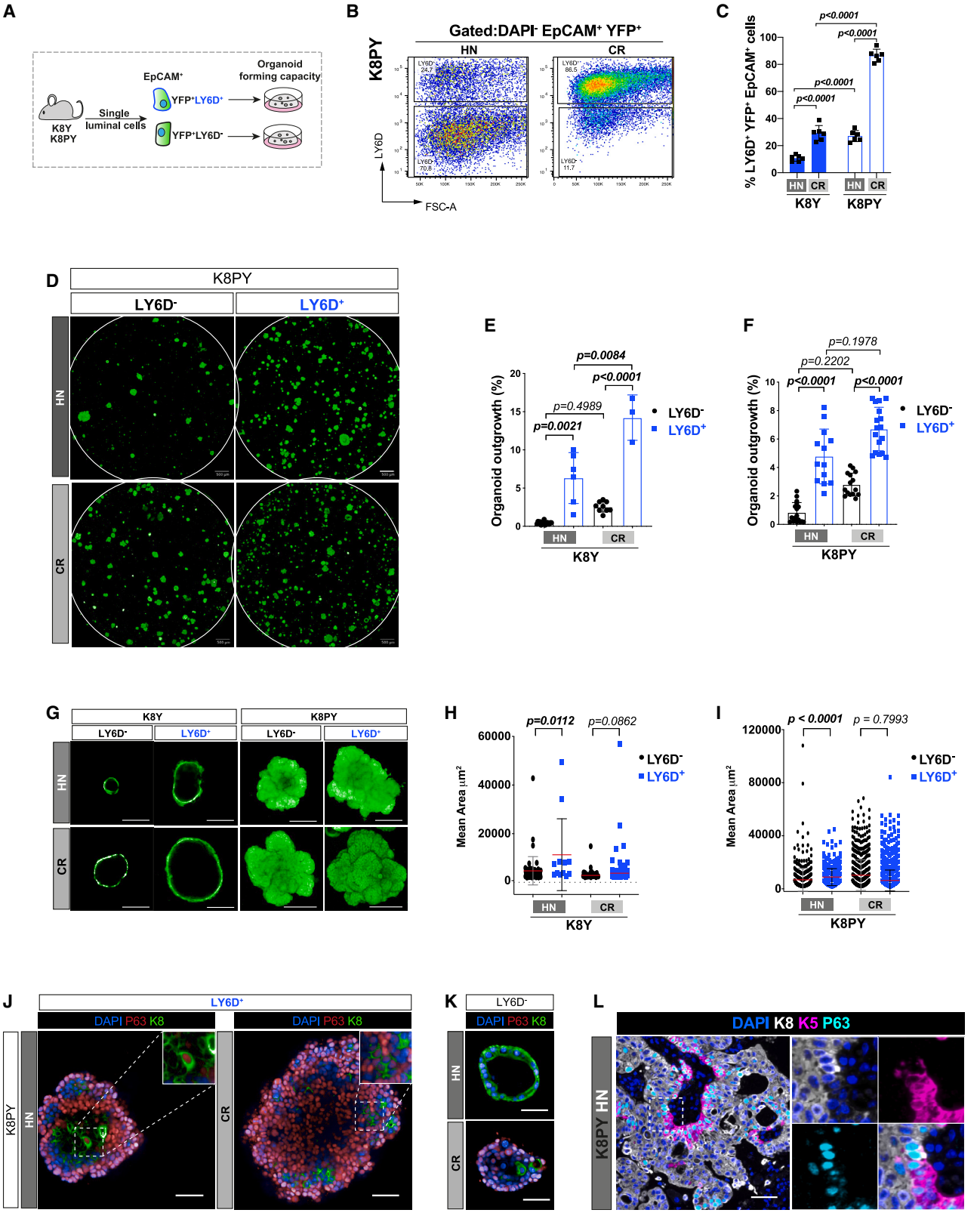

(legend on next page)

small increase in YFP$^+$LY6D$^+$ cells compared with PTEN-proficient controls; however, the total number of cells in the prostates remained comparable with those of control K8Y mice (Figures 2C and S2D). In contrast, after castration, *Pten* deletion resulted in a significant increase in the total number of prostate cells, which were also enriched for LY6D$^+$ progenitor cells, resulting in tumor lesions with a high proportion (>80%) of YFP$^+$LY6D$^+$ cells (Figures 2B, 2C, and S2D).

To assess whether the intrinsic stem properties of LY6D$^+$ luminal progenitors are maintained upon *Pten* deletion, we first evaluated their organoid-forming capacity (Figure 2D). As expected, sorted YFP$^+$LY6D$^+$ luminal cells from *Pten* wild-type control mice exhibit higher organoid-forming potential compared with LY6D$^-$ luminal cells (Figure 2E), similarly to luminal enriched SCA1^{high}LY6D$^+$ and SCA1$^{low/-}$LY6D$^+$ subsets.[6] Importantly, *Pten*-null YFP$^+$LY6D$^+$ cells also showed increased organoid-forming potential compared with their PTEN-deficient YFP$^+$LY6D$^-$ counterparts, demonstrating that LY6D marks PTEN-deficient luminal cells with higher stem potential and organoid-forming capacity (Figures 2D and 2F).

To further study the growth and proliferation potential of PTEN-deficient organoids, we assessed organoid area and symmetrical growth (roundness). YFP$^+$LY6D$^+$ progenitor-derived organoids from PTEN-proficient cells displayed a luminal-like appearance, whereas PTEN-deficient organoids showed a more tumoroid-like morphology (Figure 2G). Overall, PTEN-deficient organoids were characterized by a large area (>100 μm) and loss of a luminal-layer structure, indicated by filled lumens (Figures 2G and 2I), morphological features resembling hyperplasia of *in vivo* PIN lesions. The multi-lobular appearance of the K8PY organoids resulted in decreased roundness compared with the K8Y organoids (Figures S2F and S2G). Altogether, these data indicate that the YFP$^+$LY6D$^+$ subset is enriched in progenitor-like cells, regardless of PTEN activation and androgen stimulation.

We next assessed the lineage specificity of the *in vitro* PTEN-null organoids derived from YFP$^+$LY6D$^+$ luminal cells. Multilineage structures composed of both basal K5$^+$/p63$^+$ and luminal K8$^+$ cells were observed in organoids derived from both YFP$^+$LY6D$^+$ and YFP$^+$LY6D$^-$ luminal cells (Figures 2J and 2K). Importantly, YFP$^+$LY6D$^+$ cell-derived organoids were predominantly bipotent as indicated by double-positive (p63$^+$K8$^+$) cells (Figure 2J), in contrast to YFP$^+$LY6D$^-$ cell-derived organoids, which contained cells positive for either K8 or p63 (Figure 2K). To validate the presence of bipotent LY6D$^+$ cells *in vivo*, we stained tumor tissues from HN K8PY mice for luminal and basal markers. In keeping with our findings from *ex vivo* organoids, LY6D$^+$ cells also maintained a bipotent phenotype *in vivo*, indicated by the presence of cells positive for K8, K5, and p63 (Figure 2L).

In conclusion, our results demonstrate that LY6D distinguishes a subpopulation of CR luminal cells that are consistently enriched in stem/progenitor properties, which is maintained upon PTEN-loss-driven transformation.

PTEN-deficient LY6D$^+$ luminal tumor cells maintain a luminal progenitor-specific transcriptome

Our data establish LY6D$^+$ progenitor cells as intrinsically CR cells present not only in normal but also in transformed prostate tissues. To define how LY6D$^+$ luminal progenitor cells contribute to PCa, we performed gene expression profiling by RNA sequencing (RNA-seq) on fluorescence-activated cell sorting (FACS)-isolated YFP$^+$LY6D$^+$ and YFP$^+$LY6D$^-$ prostate luminal subpopulations, derived from PTEN-deficient mice 4 months post tamoxifen treatment (Figure 3A).

Principal-component analysis (PCA) of RNA-seq data revealed a clear distinction between LY6D$^+$ and LY6D$^-$ luminal cells derived from PTEN-deficient mice, in both HN and CR conditions (Figure 3B). The transcriptional variance across the LY6D$^+$ and LY6D$^-$ luminal cells from castrated mice was lower compared with their HN counterparts, which was expected as castration predominantly affects the transcriptional profile within the resistant subpopulations.[11] We first analyzed the transcriptional profile of LY6D$^+$ luminal cells from both HN and CR PTEN-deficient mice (Figure 3C). Differential expression analysis and gene set enrichment analysis (GSEA) revealed that the LY6D$^+$ luminal subsets only differ (false discovery rate [FDR] <0.05) in genes involved in the androgen receptor (AR) response pathway between HN and CR groups (Figures 3C and 3D). Notably, LY6D$^+$ luminal subsets from HN and CR mice had comparable *Ar* expression levels, while the expression levels of AR target genes significantly decreased upon castration (Figure 3E), indicating that these transcriptional differences were not due to variations in

Figure 2. PTEN-deficient LY6D$^+$ luminal tumor cells maintain organoid-forming capacity and castration resistance of LY6D$^+$ progenitor cells

(A) Experimental approach for the organoid culture derived from FACS-isolated cells.

(B) Representative FACS plots of LY6D expression in EpCAM$^+$ YFP$^+$ prostate cells (K8PY). HN, hormone naive; CR, castration resistant.

(C) Quantification of the LY6D$^+$ luminal cells in the DAPI$^-$ EpCAM$^+$ YFP$^+$ (gate shown in B). Data represent biologically independent replicates (n = 6, mean ± SD). Significance, two-way ANOVA, Šídák's multiple comparisons test.

(D) Maximum YFP projection images of organoid cultures derived from YFP$^+$LY6D$^+$ or YFP$^+$LY6D$^-$ sorted cells (K8PY). Scale bar, 500 μm.

(E and F) Quantification of the organoid outgrowth. Organoids derived from K8Y (E) and K8PY (F) prostates were evaluated. Data are expressed as a percentage of the organoid count. Data represent individual technical replicates from at least three biological replicates (mean ± SD). Significance, two-way ANOVA, Tukey's multiple comparisons test.

(G) Representative images of YFP$^+$LY6D$^+$- or YFP$^+$LY6D$^-$-derived organoid from control K8Y (E) or PTEN-deficient K8PY (F) prostates. Scale bar, 50 μm.

(H and I) Quantification of organoid growth (area) derived from sorted K8Y (H) and K8PY (I) luminal prostate cells. Data represent individual organoids from two biological replicates (mean ± SD). Significance, two-tailed unpaired t test with Welch's correction.

(J and K) Representative whole-mount IF of prostate K8PY-derived organoids from LY6D$^+$ (J) or LY6D$^-$ (K) luminal cells. Keratin 8 (K8, green), P63 (red). DAPI, nuclei. Scale bar, 50 μm.

(L) IF of K8PY prostates 48 weeks post tamoxifen. Tumor areas are enriched in bipotent cells (K8$^+$p63$^+$). Keratin 8 (K8, white), keratin 5 (K5, magenta), and p63 (cyan). Nuclei, DAPI. Scale bar, 50 μm. See also Figure S2.

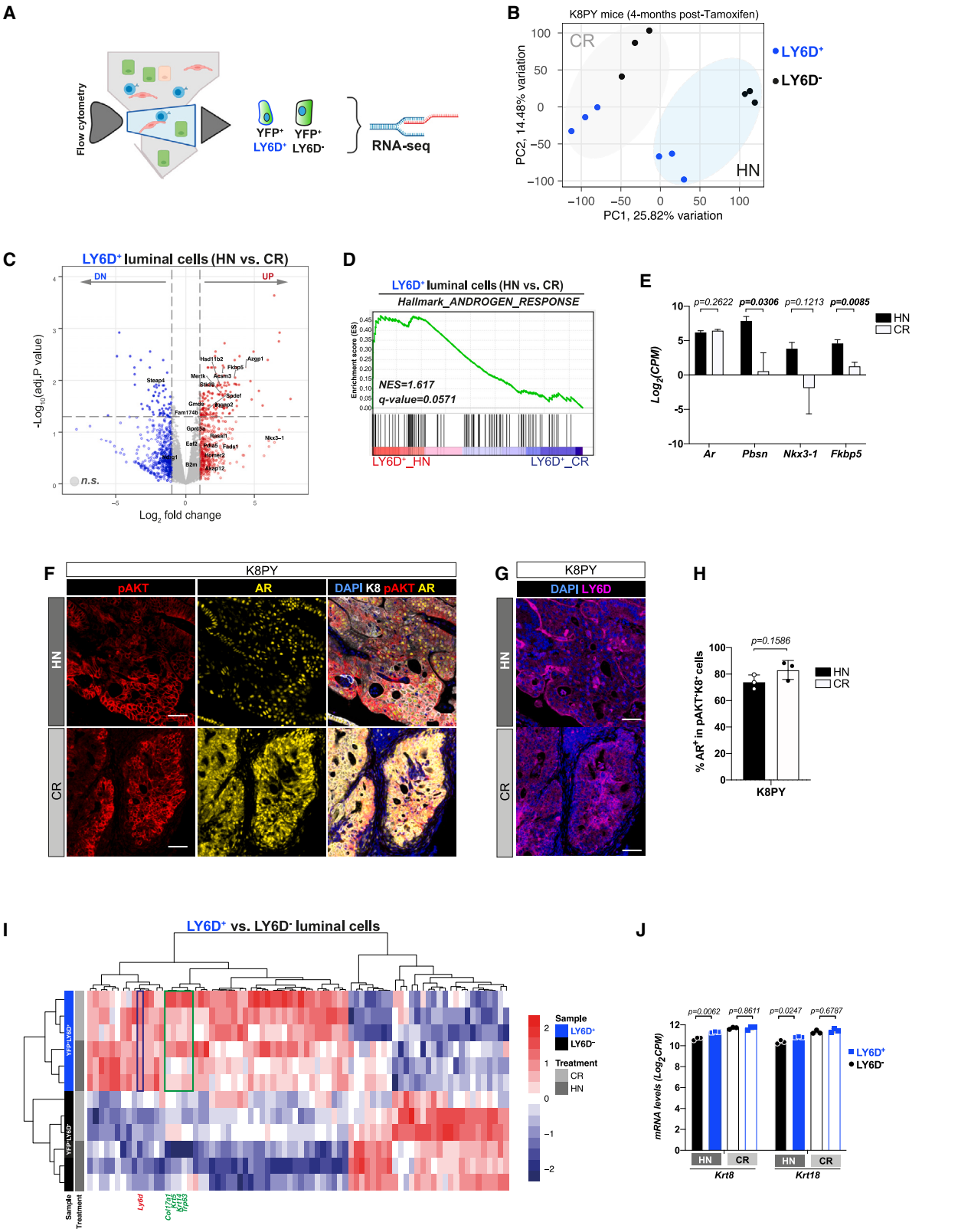

(legend on next page)

receptor gene expression. However, IF analysis of K8PY prostatic tissue revealed high AR expression in the luminal LY6D$^+$K8$^+$ PTEN-deficient tumors with a distinct distribution following castration: HN mice displayed a predominantly nuclear distribution of the AR, while castrated mice showed a diffuse cellular distribution (Figures 3F–3H).

To further define the characteristics of PTEN-deficient LY6D$^+$ luminal tumor cells, we compared their transcriptional profile with YFP$^+$LY6D$^-$ tumor cells from treatment-naive or castrated K8PY mice. Differential gene expression analysis (FDR < 0.05) revealed a conserved transcriptional program of LY6D$^+$ luminal tumor cells in both HN and CR conditions compared with their LY6D$^-$ luminal counterparts (Figures 3I and S3A). Importantly, and in keeping with our IF data (Figure 2J), PTEN-null YFP$^+$LY6D$^+$ tumor cells co-expressed basal and luminal lineage genes, indicated by high expression of *Trp63*, *Krt5*, *Krt14* and *Krt8*, *Krt18*, respectively (Figures 3I and 3J), maintaining the bipotent profile of PTEN-proficient LY6D$^+$ progenitor cells (Figures S3B and S3C).

To assess the effect of PTEN deletion on the transcriptional profile of YFP$^+$LY6D$^+$ cells, we analyzed genes differentially expressed between LY6D$^+$ cells derived from *Pten* wild-type (K8Y) and *Pten*-null (K8PY) prostates. GSEA indicated upregulation of multiple oncogenic pathways (FDR < 0.05) by PTEN deficiency in LY6D$^+$ as well as LY6D$^-$ luminal cells, including the upregulation of AKT and mammalian target of rapamycin (mTOR) pathways (Figures S3D and S3E).

Collectively, these results indicated that PTEN deficiency activated pro-tumorigenic genes in YFP$^+$LY6D$^+$ cells, which maintain their pre-existing transcriptional profile of intrinsically CR LY6D$^+$ luminal progenitors.

Distinct regulation of growth factor pathways in PTEN-deficient LY6D$^+$ luminal cells

Differential expression analysis between LY6D$^+$ and LY6D$^-$ luminal cells revealed a transcriptional pattern characteristic for each of these cell populations. To define signaling pathways orchestrating the differential gene expression, we performed ingenuity pathway analysis (IPA) of the transcriptomic profiles of luminal tumor cells. These analyses indicated a significant (FDR < 0.05) upregulation of "growth factor signaling pathways," "inflammatory response," and "integrin signaling" present in YFP$^+$LY6D$^+$ cells, conserved between HN and CR states (Figure 4A). Intriguingly, the "regulation of epithelial-mesenchymal transition (EMT) by growth factor pathway" appeared to be of particular interest to us, as both the "upregulation of the genes involved in EMT" and "activation of epidermal growth factor receptor family (ERBB)-extracellular signal-regulated kinases (ERK) pathways" have previously been associated with stemness and castration resistance.[29,30] Additionally, *ERK5*, *STAT3*, and *Phospholipase C* signaling, implicated in tumor growth and chemoresistance,[31–33] were upregulated in YFP$^+$LY6D$^+$ tumor cells, suggesting high ERK activity in these cells (Figures 4A, S4A, and S4B).

To further define canonical growth factors driving these signaling pathways, we applied GSEA to the transcriptomic data from PTEN-deficient LY6D$^+$ and LY6D$^-$ luminal cells. ERK and EGFR-PI3K signaling pathways were significantly enriched in PTEN-deficient YFP$^+$LY6D$^+$ tumor cells compared with their YFP$^+$LY6D$^-$ counterparts, in both HN and CR mice (Figure 4B). These data suggest that not only mitogen-activated protein kinase (MAPK) but also PI3K signaling may sustain LY6D$^+$ tumor cell survival *in vivo* compared with PTEN-deficient LY6D$^-$ tumor cells.

To define the underlying mechanisms contributing to the activation of EGFR/ERK pathways observed in our GSEA, we analyzed the expression of both *Erbb* family receptors and ligands in PTEN-deficient tumor cells (LY6D$^+$ versus LY6D$^-$ luminal cells). Comparative expression analysis across all conditions (HN and CR) revealed high levels of the *Erbb* family, low-affinity ligand amphiregulin (*Areg*) in YFP$^+$LY6D$^+$ luminal cells compared with LY6D$^-$ luminal cells (Figure 4C). As diverse ERBB ligands can drive differential cellular responses,[34,35] we next assessed the expression of all *Erbb* family members (Figure 4D). Importantly, we observed a significant upregulation of the EGFR ligand *Areg* and the simultaneous downregulation of *Egf* in LY6D$^+$ luminal tumor cells in all conditions. In addition, *Egfr* was minimally upregulated ($p < 0.001$) in LY6D$^+$ luminal cells from HN animals (Figure 4D). In contrast, minor or no significant changes were observed in the expression of other *Erbb* receptors (*Erbb2* and *Erbb3*) or ERBB ligands (*Tgfa*, *Btc*, *Hb-egf*), and *Erbb4* and *Ereg* were also not detected. LY6D$^+$ cells from K8Y control mice showed a concordant expression pattern of *Erbb* family members (Figures S4C–S4F). A positive correlation between *Egfr* and *Areg* expression was further demonstrated by gene expression analysis of control and PTEN-deficient

Figure 3. LY6D$^+$ tumor cells maintain a luminal progenitor transcriptome

(A) RNA-seq experimental strategy for PTEN-deficient prostate cells.

(B) PCA of YFP$^+$ luminal cells from HN or CR K8PY prostates. Each data point represents either LY6D$^+$ or LY6D$^-$ subpopulation per mouse (n = 3/group).

(C) Volcano plot showing differentially expressed genes in YFP$^+$LY6D$^+$ luminal cells in K8PY (HN versus CR). Androgen signaling-related genes are annotated.

(D) GSEA reveals positive enrichment of the hallmark androgen response in the LY6D$^+$ luminal cells from HN prostate compared with the CR counterparts. NES, normalized enrichment score. q value, FDR.

(E) RNA expression levels of *Ar* and AR-downstream genes (n = 3/group). Normalized counts per million (CPM). Log-transformed data from K8PY prostate cells RNA-seq in B).

(F) Representative IF of AR. Scale bar, 50 μm.

(G) Representative LY6D IF, K8PY prostates (HN and CR). Scale bar, 50 μm.

(H) Percentage of AR$^+$K8$^+$ cells in 48 weeks post tamoxifen K8PY prostates (HN and CR). Data represent mean ± SD, N = 3 mice/group. Significance, paired t test.

(I) Correlation-based clustering heatmap of top differentially expressed genes in LY6D$^+$ luminal tumor cells versus LY6D$^-$ luminal cells ($-1 \geq$ log-FC ≥ 1, adjusted p value < 0.05). Each column represents an individual biological replicate (n = 3/group). *Ly6d* (red), basal lineage genes (green).

(J) Luminal lineage-related genes mRNA gene expression by log-transformed normalized CPM values. *Krt8*, *keratin 8*; *Krt18*, keratin 18. Data points represent biological replicates (n = 3). See also Figure S3.

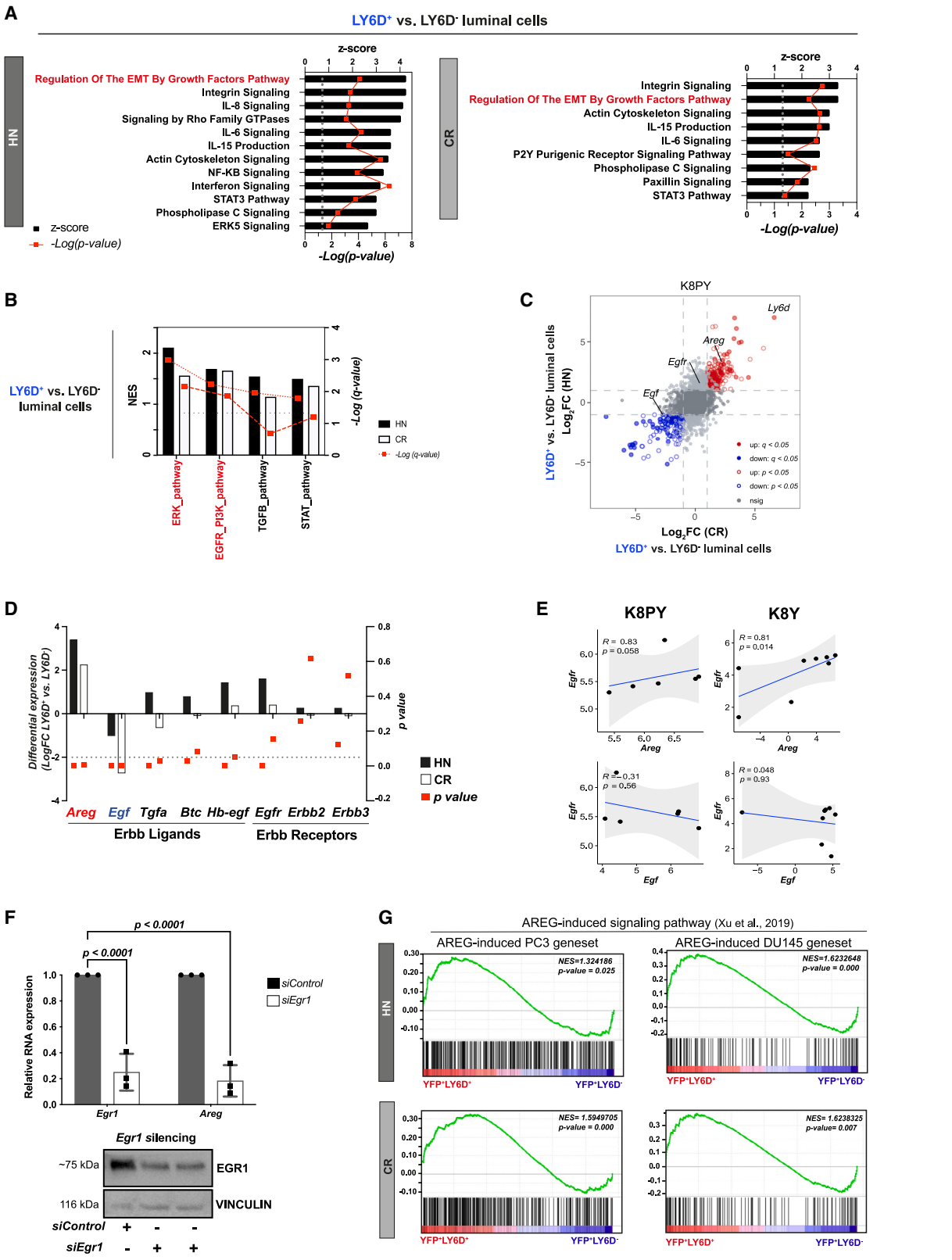

(legend on next page)

YFP$^+$LY6D$^+$ luminal cells (Figures 4E and S4C). Notably, AREG has previously been shown to inhibit epidermal growth factor (EGF) expression during tissue repair,[36] suggesting a direct inhibitory effect of AREG on EGF expression in LY6D$^+$ luminal cells. This hypothesis was further supported by our previous single-cell RNA-seq (scRNA-seq) dataset (Figure S4G[12]). Last, we assessed *Areg* and *Egf* expression in publicly available datasets from defined stages of murine prostate tumor development.[37] Notably, *Areg* levels increased with disease progression from low-grade PIN to high-grade PIN stage, while *Egf* expression levels dropped from early transformation onward (Figures S4H and S4I). We therefore hypothesize that an expansion of LY6D$^+$ tumor cells during tumor progression contributed to the observed shift between *Areg* and *Egf* ligands.

To identify transcription factors (TFs) that could govern the gene expression profiles of luminal YFP$^+$LY6D$^+$ versus YFP$^+$LY6D$^-$ subpopulations, we performed discriminant regulon expression analysis (DoRothEA).[38,39] The analysis of highest-confidence regulons (i.e., levels A and B) revealed an enrichment in the activity of 44 and 38 TFs in the HN and CR groups, respectively. Since YFP$^+$LY6D$^+$ cells are intrinsically CR cells, we focused on the common TF activity in both HN and CR luminal cells (Table S1). The TFs positively enriched (FDR < 0.05) in both HN and CR K8PY YFP$^+$LY6D$^+$ cells were mainly involved in stress and growth responses (Figure S5A), in agreement with the GSEA and IPA analysis. We then assessed whether any of those TFs may be involved in the transcriptional regulation of *Areg*, which is uniquely upregulated in PTEN-deficient YFP$^+$LY6D$^+$ cells. Further evaluation indeed revealed that *Areg* is a transcriptional target of early growth response 1 (EGR1).[40] Importantly, *Egr1* was also found to be significantly enriched in PTEN-intact K8Y luminal YFP$^+$LY6D$^+$ cells (both HN and CR; Figures S5B and S5C). Notably, silencing of *Egr1* resulted in a pronounced downregulation of *Areg* expression in prostate luminal cancer cells (Figure 4F), demonstrating that EGR1 is required for *Areg* expression. To provide corroborative evidence for this idea, we generated an AREG gene signature from a recent study (GSE116864[41]), defining the genes differentially expressed ($-1 \leq \mathrm{Log_2FC} \leq 1.5$; FDR > 0.05) on PC3 and DU145 PCa cells upon stimulation with conditioned medium (CM) from AREG-expressing stroma cells. GSEA showed the presence of an AREG-driven gene signature in PTEN-deficient YFP$^+$LY6D$^+$ luminal cells compared with LY6D$^-$ luminal cells from all conditions (HN and CR K8PY prostates) (Figure 4G). We also identified an upregulation of *EGR1* in AREG-stimulated PC3 cells (Figure S5D), suggesting a positive feedback loop between AREG and EGR1. Together, these analyses provide evidence that EGR1 is involved in AREG-mediated growth response.

Cell autonomous secretion of AREG activates MAPK signaling in LY6D$^+$ prostate cells

To test the hypothesis that AREG is an autocrine factor promoting survival and growth of LY6D$^+$ PCa cells, we first assessed AREG protein levels *in vivo* and *in vitro*. Notably, AREG can be anchored to the membrane, where it can trigger EGFR signaling in a juxtracrine manner.[42] However, membrane-anchored AREG (pro-AREG) can also be cleaved proteolytically to produce mature AREG,[43–45] a soluble form that activates EGFR through autocrine and paracrine signaling.[46,47]

In keeping with our transcriptional data, we observed significantly high AREG expression levels in *Ly6d*-expressing cells in transformed prostates from K8PY mice (Figures 5A–5C). Importantly, the expression pattern of AREG in LY6D$^+$ prostate cells varied from "nuclear" to "cytoplasmic" and "membrane," suggesting distinct molecular functions of AREG.[48,49] To assess whether AREG was actively secreted by YFP$^+$LY6D$^+$ luminal cells, FACS-sorted YFP$^+$LY6D$^+$ and YFP$^+$LY6D$^-$ cells (i.e., K8PY mice) were seeded in organoid cultures, and subsequently CM collected to evaluate AREG content (Figure S5E). After 7 days in complete mouse prostate organoid culture medium (mPOM), organoids were washed and incubated for further 24 h in growth-factor-free medium. The secreted form of AREG was measured in organoid-derived CM. Notably, we observed high levels of secreted AREG in the CM derived from YFP$^+$LY6D$^+$ organoids, in both HN and CR tumor K8PY prostate cells (Figures 5D and 5E), demonstrating that AREG is actively secreted by prostate YFP$^+$LY6D$^+$ luminal cells. IF of organoids grown in mPOM indeed confirmed that YFP$^+$LY6D$^+$ expresses AREG, which was undetectable in organoids derived from YFP$^+$LY6D$^-$ cells. Similarly, EGR1 was expressed in LY6D$^+$-derived organoids but not their negative counterparts (Figure 5F).

Primary prostate cells depend on growth factors to proliferate *in vitro* and *in vivo*, and EGF has been shown to be a key regulator for prostate organoids.[10,50] Our data suggested that LY6D$^+$

Figure 4. Growth factor pathways are uniquely enriched in PTEN-deficient LY6D$^+$ luminal cells

(A) Enriched pathway analysis (IPA, p value < 0.05) of upregulated genes in LY6D$^+$ luminal tumor cells versus LY6D$^-$ cells ($-$LogFC $\geq$1) from K8PY mice (HN or CR). Bars represent *Z* score. $-$Log(p value), red. Significance cutoff ($-$Log(p value) = 1.3), gray line.

(B) GSEA on LY6D$^+$ vs. LY6D$^-$ K8PY luminal cells on growth factor pathway-related datasets (C2-MSigDB collection). Significant upregulated datasets for both HN and CR, red. Significance cutoff: q value < 0.05.

(C) Four-way volcano plot comparing differentially expressed genes ($\mathrm{Log_2FC}$) in LY6D$^+$ versus LY6D$^-$ luminal cells from HN and CR groups (K8PY). FDR (q value) cutoff threshold, q < 0.05. $\mathrm{Log_2FC}$ (1) cutoff, gray lines.

(D) Differential expression of *Erbb* ligands and receptors ($-$LogFC) between LY6D$^+$ and LY6D$^-$ luminal cells. Line, significance cutoff (p value = 0.05).

(E) Receptor-ligand Spearman's correlation analysis between *Egfr* (receptor) and ligands (*Areg* or *Egf*) in YFP$^+$LY6D$^+$ luminal cells. R, rank correlation coefficient. Significance cutoff (p value < 0.05). *Areg*, amphiregulin.

(F) Relative RNA expression of *Areg* and *Egr1* measured by RT-qPCR after silencing *Egr1* (*siEgr1*) in PCa luminal cells for 7 days. Non-targeting siRNAs (*siControl*). B-actin was used for normalization. Data represent three independent experiments (mean ± SD). Two-way ANOVA, Dunnett's multiple comparisons test was used. EGR1 protein was measured by western blot. Vinculin, loading control.

(G) GSEA evaluating AREG-induced signaling pathway, on YFP$^+$LY6D$^+$ and YFP$^+$LY6D$^-$ luminal cells from K8PY mice. AREG-induced PC3 and DU145 genesets, extracted from GSE116864. K8PY (PTEN deficient) and K8Y (control). FC, fold change. See also Figures S4 and S5, and Table S1.

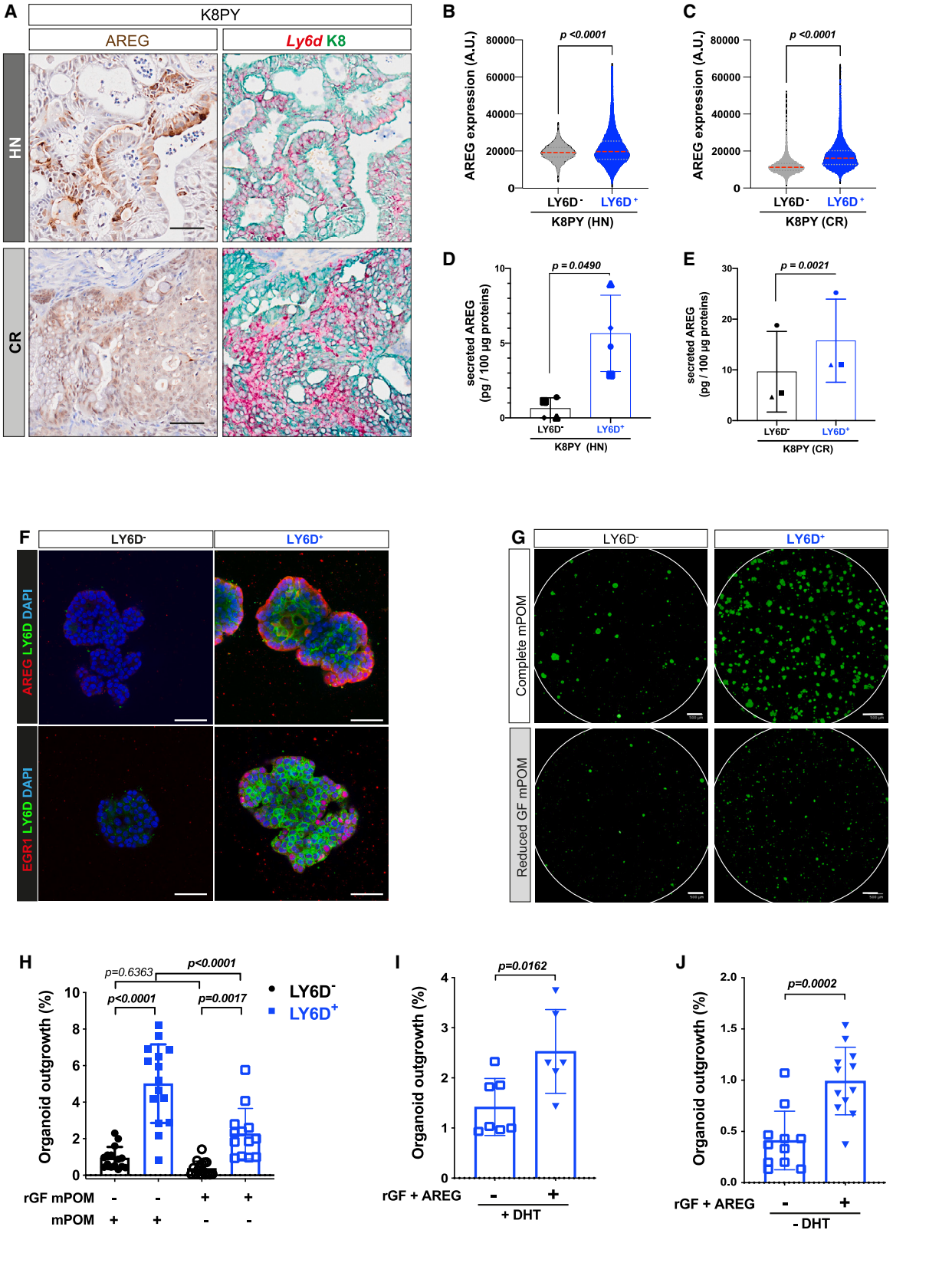

(legend on next page)

luminal cells may be less dependent on exogenous growth factors due to their capacity to endogenously secrete growth factors such as AREG. To test this hypothesis, sorted LY6D$^+$ and LY6D$^-$ luminal cells were seeded in either complete mPOM (also containing EGF) or in reduced growth factor (rGF) medium without EGF (rGF medium). Strikingly, YFP$^+$LY6D$^+$ luminal cells derived from HN K8PY mice were able to grow organoids under reduced growth conditions. Although a lower organoid-forming capacity in rGF conditions, YFP$^+$LY6D$^+$ luminal cells maintained a growth advantage compared with YFP$^+$LY6D$^-$ cells (Figures 5G and 5H). A similar result was observed in CR K8PY-derived organoids (Figures S5F and S5G). Importantly, AREG supplementation to rGF medium further promoted organoid outgrowth from YFP$^+$LY6D$^+$ cells, irrespective of androgen stimulation (Figures 5I and 5J).

These results demonstrate that YFP$^+$LY6D$^+$-derived AREG secretion promotes organoid formation, which is maintained even in the absence of exogenous growth factors.

Targeting AREG/EGFR/ERK signaling impairs growth of CR LY6D$^+$ prostate cells

Our data indicate the presence of a constitutive activation of the AREG/EGFR/EGR1 signaling pathway in LY6D$^+$ luminal tumor cells. To mechanistically delineate how AREG promotes growth and survival, we investigated AREG signaling in DVL3 cells, a recently established mouse cell line from a treatment-naive PTEN/TP53 prostate adenocarcinoma.[51] Stimulation of cells with exogenous AREG resulted in the rapid phosphorylation of EGFR at Tyr 1086 and Tyr 845 sites (Figures S6A and S6B), but not at Tyr 992, which is known to be activated by EGF.[35] Further downstream, ERK1/2 is phosphorylated by AREG (Figures S6A and S6C), while activation of AKT was unaffected. Notably, protein levels of EGR1 also increased shortly after AREG stimulation in DVL3 tumor cells (Figures S6A and S6D), suggesting posttranslational stabilization of EGR1 by AREG. AREG-mediated ERK1/2 activation and EGR1 upregulation could be suppressed by pretreatment of cells with the MEK inhibitor trametinib (Figures 6A, and S6E). Similarly, erlotinib also inhibited AREG-mediated ERK activation and EGR1 upregulation (Figures S6F–S6I).

To test whether autocrine AREG promotes cell survival, DVL3 were plated in BME2 matrix in the presence or absence of androgen stimulation (i.e., ±dihydrotestosterone [DHT]) in three conditions: rGF mPOM (lacking EGF), rGF with EGF (equivalent to complete mPOM), and rGF with AREG (Figure S6J). Upon 3D culture of DVL3 in mPOM, cells upregulated AREG and LY6D, further supporting the association between these genes (Figure S6K). We then assessed the levels of secreted AREG in CM from LY6D$^+$-enriched DVL3 cells, in the absence or presence of EGF or AREG. Both EGF and AREG further increased secretion of AREG (Figure S6L). Notably, the levels of secreted AREG were much higher upon AREG stimulation irrespective of androgen stimulation (Figure S6L). To test whether induced AREG levels were transcriptionally regulated, we assessed their RNA expression levels (Figure S6M). In keeping with our ELISA data, *Areg* transcript levels increased by stimulating cells with EGF or AREG, while *Egf* levels remained unchanged (Figure S6M). IF analysis further confirmed the expression of AREG in LY6D$^+$ DVL3 prostate tumor cells (Figure S6N). Similarly, *Egr1* mRNA levels increased upon AREG stimulation in the presence and absence of androgens, while its levels decreased by EGF stimulation in HN conditions (Figure S6M). Collectively, these data demonstrate that AREG stimulates its own expression, establishing an autonomous, self-amplifying signaling loop involving activated MAPK, irrespective of androgen stimulation.

To determine a functional role for AREG-induced MAPK signaling for cell growth, we treated LY6D-enriched DVL3 cells with MAPK inhibitors and then assessed their organotypic growth in 3D cultures. Blockage of MAPK signaling significantly inhibited organotypic outgrowth of DVL3 cells (Figures 6B, 6C, and S6O). Notably, under androgen-deprived conditions, inhibition of EGFR signaling further compromised outgrowth of LY6D-enriched DVL3 cells (Figures 6B, 6C, and S6O). To evaluate whether the effects of MAPK inhibition extend to intrinsically CR primary tumor cells, we analyzed outgrowth of organoids in isolated, PTEN-deficient YFP$^+$LY6D$^+$ and YFP$^+$LY6D$^-$ tumor cells. In keeping with our cell-line data, blockade of MAPK signaling with trametinib almost completely abrogated cell growth of both LY6D$^+$ and LY6D$^-$ primary prostate cells, but these effects were significantly more pronounced in LY6D$^+$ tumor cells due to their intrinsic growth advantage in the absence of androgen (Figures 6D–6F). These data provide direct evidence

Figure 5. Amphiregulin secretion regulates MAPK signaling

(A) Representative staining showing AREG expression in K8PY prostates (left). *Ly6d* (RNA-ISH) is co-expressed in the AREG rich regions (right).

(B) Quantification of AREG expression in luminal *Ly6d*-expressing K8$^+$ cells and their *Ly6d*-negative counterparts in the prostate from K8PY HN mice. Data points represent individual cells (n = 3). Two-tailed paired t test was used for the statistical analysis.

(C) Quantification of AREG expression in luminal *Ly6d*-expressing K8$^+$ cells and their *Ly6d*-negative counterparts in the prostate from K8PY castrated (CR) mice. Data points represent individual cells from biological replicates (n = 3). Significance, two-tailed paired t test.

(D and E) Quantification of CM-secreted AREG from YFP$^+$LY6D$^+$- or YFP$^+$LY6D$^-$-derived organoids from K8PY HN (D) and CR (E) mice. Data points represent biological replicates (n = 3, mean ± SD). Significance, paired t test.

(F) Representative IF of AREG or EGR1 in YFP$^+$LY6D$^+$- or YFP$^+$LY6D$^-$-derived organoids from K8PY males. AREG, red; EGR1, red; LY6D, green. Nuclei, DAPI. Scale bar, 50 μm.

(G) Maximum YFP projection images of LY6D$^+$ or LY6D$^-$ luminal cell-derived organoids from HN K8PY males, grown in complete mPOM or rGF mPOM medium. Scale bar, 500 μm.

(H) Quantification of the organoid outgrowth as in (G). Data are expressed as percentage of the organoid count. Data represent individual technical replicates from four biological replicates (mean ± SD). Significance, two-way ANOVA, Tukey's multiple comparisons test.

(I) Organoid outgrowth of LY6D$^+$ luminal-cell-derived organoids in the presence or absence of growth factor (AREG) in the presence of androgen stimulation (+1 nM DHT). Data represent individual technical replicates from two biological replicates (mean ± SD). Significance, independent t test.

(J) Organoid outgrowth of LY6D$^+$ luminal-cell-derived organoids in the presence or absence of growth factor (AREG) under androgen-deprived conditions (−DHT). Data represent individual technical replicates from three biological replicates (mean ± SD). Significance, unpaired t test. DHT,. See also Figure S5.

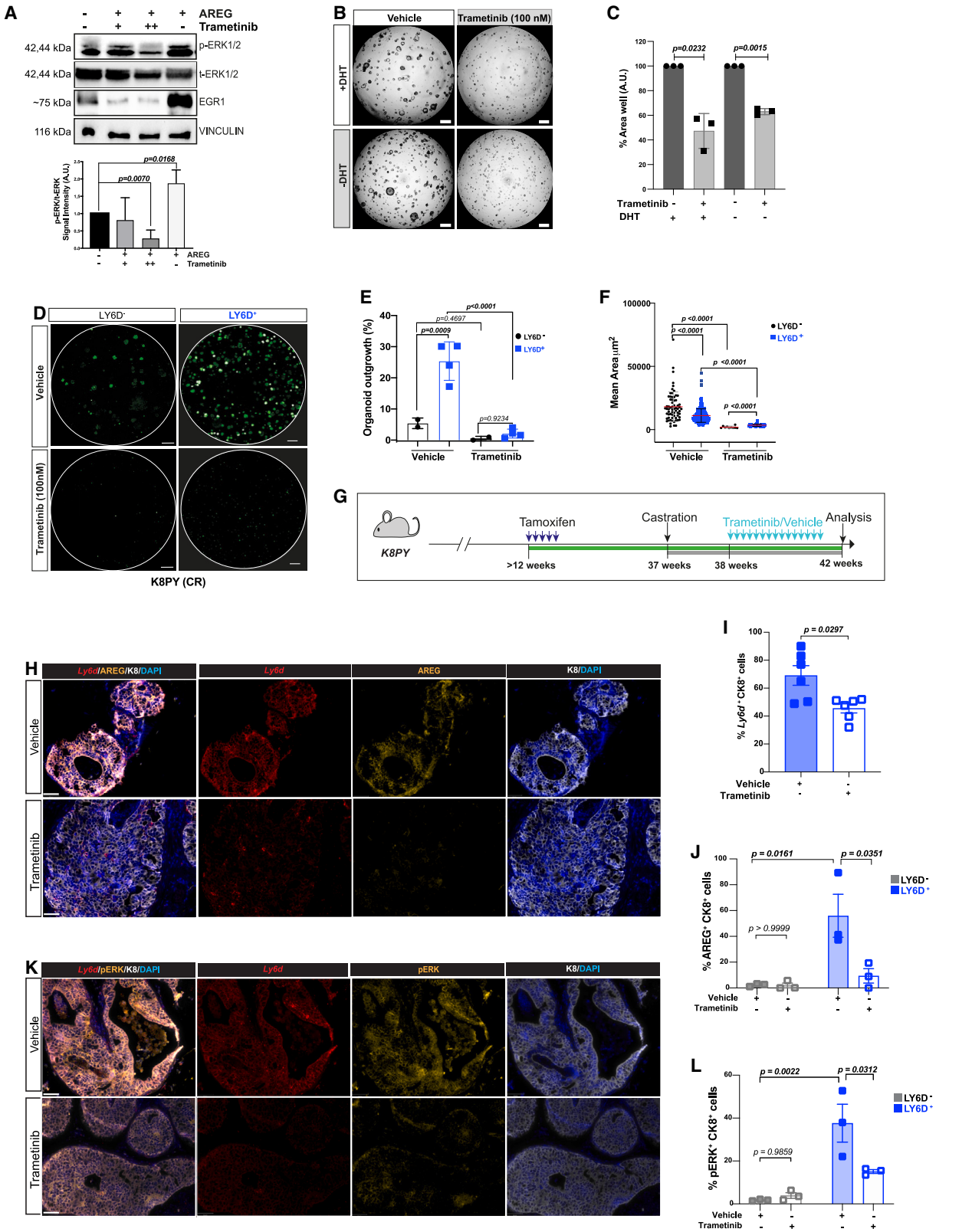

(legend on next page)

that EGFR signaling is augmented by autocrine AREG secretion, regulating cell growth of CR LY6D$^+$ prostate tumor cells.

To further assess the relevance of MAPK signaling for the propagation of LY6D$^+$ cancer cells, we treated tumor-bearing PTEN-deficient K8PY mice for 4 weeks with trametinib. Mice were castrated 1 week prior to trametinib treatment to test whether MAPK inhibition is therapeutically meaningful in addition to androgen deprivation (Figure 6G). Assessment of LY6D$^+$ cells in K8PY mice showed that MAPK inhibition significantly reduced the number of LY6D$^+$ cells in castrated animals (Figures 6H and 6I), associated with a marked reduction of AREG and pERK (Figures 6H and 6J–6L), indicating the presence of an autocrine stimulation of LY6D$^+$ cells *in vivo*, which depends on MAPK signaling. Altogether these data provide evidence for the presence of an AREG-dependent autocrine feedback loop, required for the survival of LY6D$^+$ cells.

Human LY6D$^+$ prostate tumor cells are present post androgen-deprived therapy

Our PCa preclinical data suggested that LY6D$^+$ luminal cells contribute to androgen resistance in human PCa. Accordingly, we previously demonstrated the presence of LY6D$^+$ cells in human normal and tumor prostate tissues,[6] but their abundance in malignant tissues so far remained unknown. We speculated that the high level of intra- and interpatient heterogeneity of PCa[1,3,4] could possibly affect the abundancy of LY6D$^+$ cells in PCa tumor samples. To account for this, we built a tissue microarray (TMA) capturing the multifocality of prostate tumors (Figures S7A and S7B; Table S2). Multiplex IF analyses identified expression of LY6D in prostate epithelial cells marked by cytokeratin (CK) and prostate-specific membrane antigen (PSMA) in most core samples (Figures 7A and S7A). Notably, the expression pattern of LY6D in the normal tissue was sparse and focal (Figure 7A, and[6]). Importantly, we observed a strong correlation between LY6D and AREG staining (Figure 7B). We next extended our analyses to lymph node metastasis derived from patients undergoing extended prostatectomy and pelvic lymphadenectomy. In nine out of 10 patient samples, LY6D$^+$ prostate cells were also present in the lymph node metastasis with variations in their frequencies compared with the primary tissue (Figures 7B–7D). Notably, since these patients were HN, no evolutionary pressure existed for the selection of CR cells. Further analyses of LY6D expression and Gleason scores of the respected tissue area indicated a correlation between LY6D and higher Gleason scores (Figure 7D), supporting the hypothesis that LY6D$^+$ cells significantly contribute to PCa progression.

Based on our previous data and the autocrine survival loop of LY6D$^+$ luminal cells described here, we hypothesized that castration of PCa patients further selects for survival of intrinsically CR, LY6D$^+$ luminal cells. To test this, we obtained matching longitudinal biopsies from three PCa patients at the time of their diagnosis and after androgen deprivation therpay (ADT) (Table S3). Similar to our results from treatment-naive tissues from prostatectomies (Figures 7A–7C), we identified LY6D$^+$ cells in all biopsies (Figures 7E and S7C). Importantly, 6 months after ADT, LY6D$^+$ tumor cells were the dominant cell population in two out of three samples, indicative of their *in vivo* selection by ADT (Figures 7F and S7E).

In conclusion, our data demonstrate that a substantial fraction of tumor cells in HN patients express LY6D, and their frequency correlates with higher Gleason grades. Furthermore, the selective pressure imposed by ADT favors the outgrowth of LY6D$^+$ cells *in vivo* and in keeping with our preclinical data.

DISCUSSION

Resistance to androgen deprivation remains a clinical challenge for patients with PCa and is the main cause for death of patients

Figure 6. Inhibition of MAPK signaling to target LY6D$^+$ tumor cells

(A) AREG-stimulated DVL3 cells were analyzed after trametinib treatment: (−) vehicle (DMSO), (+) 25 nM, or (++) 50 nM. Immunoblot analysis of phosphorylation of ERK1/2 (pERK), EGR1 and vinculin loading control 24 h post-trametinib. Quantification of pERK/ERK for the indicated treatments. Data represent at least three independent experiments (mean ± SD). Significance, unpaired t test.

(B) Organotypic 3D cultures of DVL3 prostate cells were treated with trametinib (100 nM) for 4 days. Control cells were treated with vehicle (DMSO) in the presence (+DHT, 1 nM) or absence (−DHT) of androgen stimulation. Whole-well brightfield images. Scale bar, 500 μm.

(C) Quantification of the organotypic DVL3 cultures shown in (B). Treatment effect shown as percentage of the covered area. Data represent independent experiments (n = 3, mean ± SD). Significance, paired t test.

(D) Primary LY6D$^+$ or LY6D$^-$ prostate tumor-cell-derived organoids treated with vehicle or trametinib (100 nM) collected at endpoint (5 days post treatment). Scale bar, 500 μm.

(E) Quantification of the organoid outgrowth from sorted K8PY CR cells shown in (D). Data represent individual organoids from two biological replicates (mean ± SD). Significance, two-way ANOVA with Dunnett correction.

(F) Quantification of trametinib treatment on tumor organoid growth (area) shown in (D). Data represent individual organoids from two biological replicates (mean ± SD). Significance, two-way ANOVA with Dunnett correction.

(G) Experimental timeline to evaluate MAPK inhibition (i.e., trametinib) of PTEN-deficient K8PY tumor model.

(H) AREG expression in mouse prostates from K8YP mice treated with vehicle and trametinib. *Ly6d* (RNA-ISH, red), AREG (yellow), keratin 8 (K8, white). Nuclei, DAPI.

(I) Quantification of *Ly6d*-expressing luminal (*Ly6d*$^+$ K8$^+$) cells in mouse prostates from treated K8YP mice (vehicle or trametinib). Data represent technical replicates (n = 3, two sections per mouse, mean ± SD). Significance, unpaired t test.

(J) Quantification of AREG-expressing cells within the LY6D$^+$ (*Ly6d*-expressing) and LY6D$^-$ (*Ly6d*-negative) luminal cells in mouse prostates from treated K8YP mice. Data represent individual biological replicates (n = 3, mean ± SD). Significance, two-way ANOVA with Šídák's correction.

(K) MAPK activity measured by pERK in mouse prostates from K8YP mice treated with vehicle and trametinib.

(L) Quantification of pERK-expressing cells within the LY6D$^+$ (*Ly6d*-expressing) and LY6D$^-$ (*Ly6d*-negative) luminal cells in mouse prostates from treated K8YP mice. Data represent individual biological replicates (n = 3, mean ± SD). Significance, two-way ANOVA with Tukey's correction. See also Figure S6.

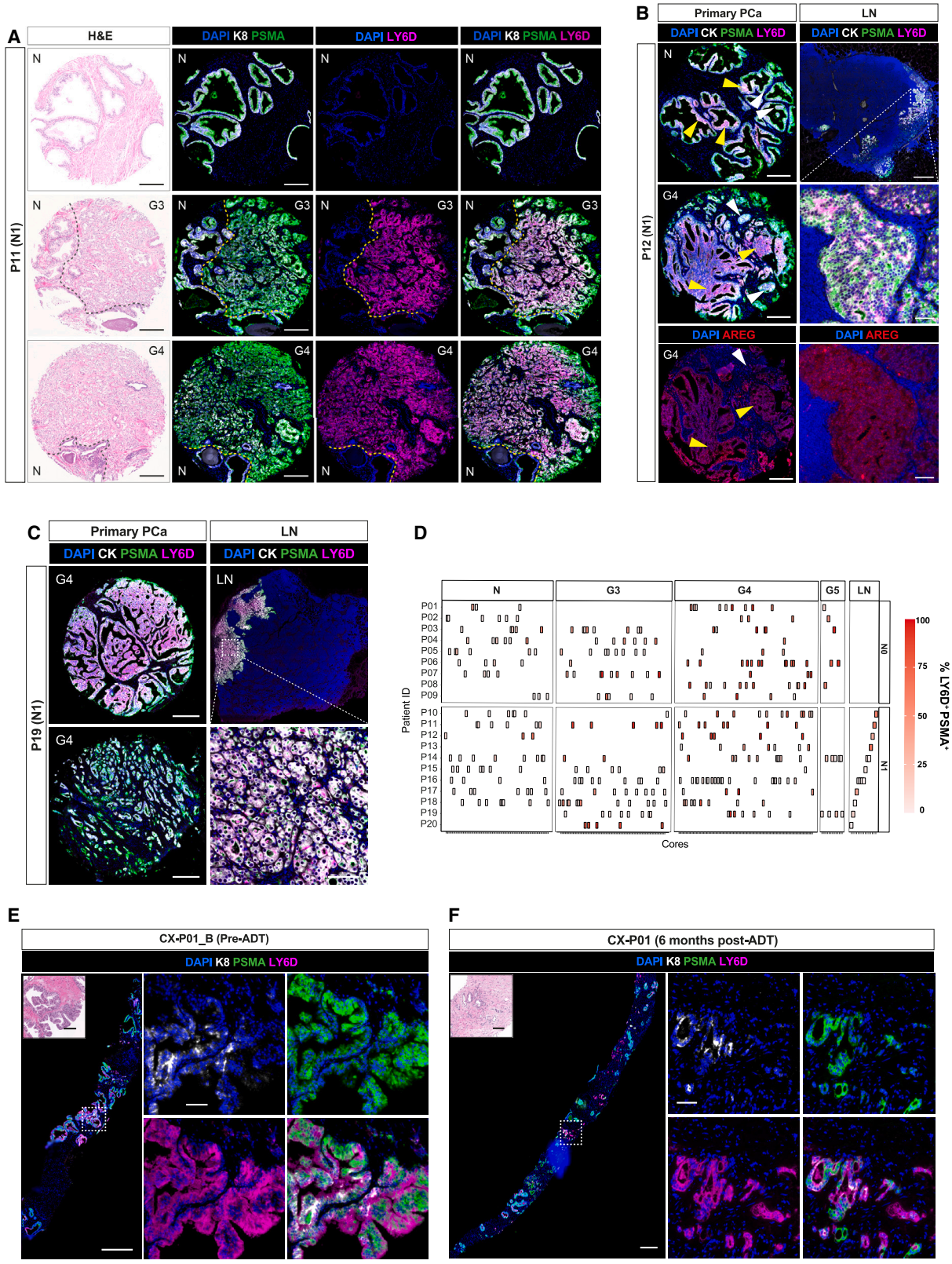

(legend on next page)

with advanced PCa. We have previously defined that LY6D marks a population of intrinsically CR luminal stem/progenitor cells present in normal, non-malignant tissues. We here identified an autocrine signaling loop, present in LY6D$^+$ luminal progenitor cells, which provides survival signals through AREG-mediated MAPK signaling.

The presence of different subsets of prostate progenitor cells in the adult prostate, their spatial distribution (proximal versus distal), and their contribution to human PCa remain controversial. Recent studies indeed suggest a differential function of co-existent luminal progenitors.[8,9,11,12,24,52–54] Notably, the frequency of distal progenitors increases with age,[52] as does the content of somatic mutations in the peripheral zone,[55] suggesting a role also of distal environment in tumor initiation. From early stages of development[12] to adulthood, we observed LY6D$^+$ progenitor cells scattered in both proximal and distal regions. Notably, in adult male mice (>12 weeks old) the intrinsically CR LY6D$^+$ luminal population was preferentially located in distal regions. Interestingly, some studies have reported high *Ly6d* expression only in the proximal and periurethral regions of the prostate,[8,11,16] which may in part be due to the higher number of LY6D$^+$ progenitors in the proximal area in young mice (1–3 months). We here describe the presence of LY6D$^+$ prostate cells in the human androgen-ablated prostate epithelium, further validating our findings in our luminal PCa mouse model. This finding strongly supports the idea that preferentially distal LY6D$^+$ luminal cells initiate and drive aggressive prostate tumors.

Our RNA-seq analysis to define the underlying mechanisms of CR revealed that CR LY6D$^+$ tumor cells maintain the expression of *Ar*; however, downstream signaling was ablated. In contrast, the EGFR-MAPK pathway was uniquely upregulated in LY6D$^+$ luminal progenitors in the absence of androgen, supporting the hypothesis that MAPK activation is an intrinsic mechanism of resistance to androgen deprivation. Our transcriptomic data provide evidence that LY6D$^+$ luminal PCa progenitors express high levels of AREG and simultaneously downregulate *Egf*. AREG secretion by LY6D$^+$ luminal cells leads to an autocrine stimulation, promoting cell growth and survival in the absence of androgen and adding to the complexity of Erbb ligand dynamics for the regulation of adult stem and progenitor cells.[56] Similar to the role of AREG in regulating LY6D$^+$ luminal cells described here, AREG is essential for the development of the mammary gland through an interaction with estrogen receptor (ER) signaling[57] and progression of ovarian cancer.[58] In keeping with our data, ERBB receptors and their ligands have previously been proposed to compensate for the absence of androgen signaling in PCa.[59,60]

During PCa tumorigenesis, increased expression of AREG has been observed with disease progression.[61] Furthermore, an upregulation of AREG was observed following androgen deprivation in the PCa xenografts,[62] suggesting an increased presence of CR cells in the developing PCa. Our finding that the autocrine AREG stimulatory loop, present in LY6D$^+$ tumor cells, is regulated by the EGR1 TF is consistent with previous studies showing that aberrant expression of AREG in keratinocytes and breast cancer cells can stimulate EGFR and trigger the activation of ERK and EGR1.[63,64] Similarly, the upregulation of EGR1 has been associated with increased Gleason grade and progression to metastasis.[65,66] Notably, EGR1 expression can be modulated by mutated TP53, adding further complexity to its role in cancer cells.[67] While these studies clearly support the idea of AREG as a driver of castration resistance and that the AREG-EGR1 axis may be part of a more complex mechanism, it hitherto remained unknown which subset of prostate cells predominantly contribute to this. Our data demonstrating that LY6D$^+$ cells express high levels of AREG provide further details on the source of AREG in PCa and indicate a therapeutic angle to interfere with the expansion of AREG$^+$ cells.

Multiple efforts to characterize the biology associated with aggressive PCa have aimed at developing targeted therapies. Notably, the clinical and molecular heterogeneity of PCa and the lack of recurrent driver mutations in a substantial proportion of patients are obvious hurdles for stratified, randomized clinical trials, exemplified by a recently published phase III trial combining an AKT inhibitor and ADT: while preclinical and early clinical data suggested that this combination is active in PTEN-deficient PCa,[68] the placebo-controlled phase III trial did not observe a benefit for the intention-to-treat population.[69] Our results support an alternative approach by using MAPK inhibitors in combination with anti-androgen therapy to prevent the emergence of CR PCa (CRPC). Targeting of the AREG/EGFR axis could be a meaningful way to eradicate intrinsically CR cells, driving disease progression. While directly antagonizing AREG seems more difficult due to its secretion, interference with its activated signaling pathway is possible through the use of EGFR and MAPK inhibitors.[70] In line with this hypothesis, EGFR has previously been identified as a potential target for the treatment of PCa.[71,72] However, small-molecule tyrosine kinase inhibitors, including erlotinib, lapatinib, and gefitinib, have

Figure 7. Presence of LY6D$^+$ cells in localized and metastatic patient samples

(A) Representative H&E and IF images of distinct histopathology in patient 11 (P11(N1)). LY6D (magenta), PSMA (green), prostate epithelia (keratin 8 [K8]). Nuclei, DAPI. Scale bar, 200 μm. Dashed line demarked normal (N) regions. N, normal; G, Gleason score.

(B) Representative IF images of patient 12 (P12): primary PCa (left) and lymph node (LN) metastases (right), showing high LY6D and AREG expression. Scale bar, 200 μm (left), LN sections (top, 500 μm; 50 μm). LY6D (magenta); PSMA (green); CK (white); AREG (red). Nuclei, DAPI. White arrows, LY6D-negative regions. Yellow arrows, LY6D-positive regions.

(C) Representative IF images of intertumoral heterogeneity in primary PCa. LN sections showing enrichment of LY6D$^+$ tumor cells. Scale bar, 200 μm (left), LN sections (top, 500 μm; bottom, 50 μm).

(D) Quantification of percentage of cells displaying expression of LY6D in the prostate epithelium (CK$^+$PSMA$^+$) from PCa patients (N0 or N1). N0, patients without LN metastases; N1, patients with LN metastases.

(E and F) Representative H&E and IF images from needle core biopsies collected from PCa patient CX-P01 before (E) and after (F) androgen deprivation therapy (post ADT). Nuclei, DAPI, K8 (white), PSMA (green), and LY6D (magenta). Scale bar, H&E (100 μm), IF (left, 500 μm; right, 50 μm). See also Figure S7, and Tables S2 and S3.

shown limited effectiveness in treating CRPC as a single agent or in combination with chemotherapy.[73–79] Again, these poor responses likely reflect the molecular complexity of advanced metastatic CRPC. Importantly, patients entering these clinical trials were not stratified based on the expression levels of EGFR or receptor ligands, which could have affected the overall efficacy of such therapies. More encouraging data have recently emerged from a phase I trial in refractory, metastatic CRPC patients treated with trametinib, demonstrating improved overall survival.[80] Additional phase II trials are underway testing the efficacy of trametinib for the treatment of advanced PCa (NCT01990196, NCT02881242). Our *in vivo* data indicate that inhibiting MAPK signaling synergizes with androgen deprivation by interrupting an AREG-driven autocrine feedback loop and suggest that early treatment with MAPK inhibitors may substantially delay or even suppress the emergence of CRPC. Furthermore, our data indicate that intrinsically CR cells can be detected in biopsies by staining for LY6D, long before the initiation of androgen deprivation therapies. This may potentially allow for a preemptive treatment before the emergence of a clinically apparent disease resistant to androgen deprivation. For a clinical trial, LY6D expression may indeed be a meaningful biomarker for the clinical development of a combination therapy.

Together, our study highlights a key mechanism underlying intrinsic castration resistance in prostate cells. Our findings provide a rationale to target pre-existent CR localized tumors before the emergence of resistant disease by combining androgen-deprivation therapies with emerging approaches to eliminate LY6D$^+$ cells, either with anti-EGFR therapy or the potential use of monoclonal antibodies against LY6D. Clinical trials are warranted to address whether these findings can be translated into improved patient care.

Limitations of the study

We here report an inherent mechanism of resistance to androgen deprivation of LY6D luminal prostate cells using an *in vivo* mouse tumor-tracing model. While our findings demonstrate activation of the MAPK-signaling pathway by an autocrine AREG-mediated feedback loop in LY6D$^+$ luminal tumor cells as the key mechanism underlying cell survival, other mechanisms sustaining CR LY6D$^+$ tumor cells cannot be ruled out. Results from our mouse model experiments translate to patients as LY6D expression is associated with higher Gleason scores and poorer clinical outcome. However, the area biopsied may limit the identification of LY6D-resistant cells in PCa patients due to the high heterogeneity underlying PCa specimens. In addition, we have used a limited number of patients in our analyses, and therefore bigger cohorts of treatment-naive metastatic patients need to be analyzed to fully assess the contribution of LY6D$^+$ cells for advanced PCa.

STAR★METHODS

Detailed methods are provided in the online version of this paper and include the following:

SUPPLEMENTAL INFORMATION

Supplemental information can be found online at https://doi.org/10.1016/j.celrep.2023.112377.

ACKNOWLEDGMENTS

We thank all members of the Prostate Oncobiology Lab for helpful discussions. The authors thank colleagues in the CRUK Manchester Institute Core facilities (Biological Resources Unit, Transgenic breeding, Molecular Biology, Histology, Flow Cytometry and Visualization) for their help. Research patient samples were obtained from the Manchester Cancer Research Centre (MCRC) Biobank, UK. Finally, we thank patients for donating their samples. This study was supported by funds from CRUK Manchester Institute to E.B. (C5759/A20971), funds from Prostate Cancer UK-Movember Prostate Cancer Centre of Excellence grant (CE013_2-004), and by CRUK via funding to the Cancer Research Manchester Centre (C147/A25254). A.C. is supported by the NIHR Manchester Biomedical Research Centre. The graphical abstract was created with images from BioRender.com.

AUTHOR CONTRIBUTIONS

I.S. and T.N.J.F.T. planned and conducted the experiments, analyzed the data, and wrote the manuscript. I.G.M., S.M., D.M.Z., A.C., and G.L. provided experimental advice. I.S., T.N.J.F.T., R.M., and P.W. performed the *in vivo* experiments. I.S., T.N.J.F.T., P.S., N.F., and S.M. performed bioinformatics analysis. I.S. and A.A. performed immunohistochemistry analysis in patient tissues. P.O. performed pathology analysis in patient tissues. C.T. and A.C. provided AToM clinical specimens. I.S., T.N.J.F.T., C.B., G.A., and P.O. supervised immunohistochemistry experiments. E.B. conceived the project, analyzed the data, provided oversight, and wrote the manuscript. All authors reviewed the manuscript.

DECLARATION OF INTERESTS

All authors declare no competing interests.

INCLUSION AND DIVERSITY

We support inclusive, diverse, and equitable conduct of research.

Received: November 5, 2021
Revised: December 12, 2022
Accepted: March 23, 2023
Published: April 14, 2023

REFERENCES

1. Boutros, P.C., Fraser, M., Harding, N.J., de Borja, R., Trudel, D., Lalonde, E., Meng, A., Hennings-Yeomans, P.H., McPherson, A., Sabelnykova, V.Y., et al. (2015). Spatial genomic heterogeneity within localized, multifocal prostate cancer. Nat. Genet. *47*, 736–745. https://doi.org/10.1038/ng.3315.

2. Cooper, C.S., Eeles, R., Wedge, D.C., Van Loo, P., Gundem, G., Alexandrov, L.B., Kremeyer, B., Butler, A., Lynch, A.G., Camacho, N., et al. (2015). Analysis of the genetic phylogeny of multifocal prostate cancer identifies multiple independent clonal expansions in neoplastic and morphologically normal prostate tissue. Nat. Genet. *47*, 367–372. https://doi.org/10.1038/ng.3221.

3. Haffner, M.C., Mosbruger, T., Esopi, D.M., Fedor, H., Heaphy, C.M., Walker, D.A., Adejola, N., Gürel, M., Hicks, J., Meeker, A.K., et al. (2013). Tracking the clonal origin of lethal prostate cancer. J. Clin. Invest. *123*, 4918–4922. https://doi.org/10.1172/jci70354.

4. Parry, M.A., Srivastava, S., Ali, A., Cannistraci, A., Antonello, J., Barros-Silva, J.D., Ubertini, V., Ramani, V., Lau, M., Shanks, J., et al. (2019). Genomic evaluation of multiparametric magnetic resonance imaging-visible and -nonvisible lesions in clinically localised prostate cancer. Eur. Urol. Oncol. *2*, 1–11. https://doi.org/10.1016/j.euo.2018.08.005.

5. Agarwal, S., Hynes, P.G., Tillman, H.S., Lake, R., Abou-Kheir, W.G., Fang, L., Casey, O.M., Ameri, A.H., Martin, P.L., Yin, J.J., et al. (2015). Identification of different classes of luminal progenitor cells within prostate tumors. Cell Rep. *13*, 2147–2158. https://doi.org/10.1016/j.celrep.2015.10.077.

6. Barros-Silva, J.D., Linn, D.E., Steiner, I., Guo, G., Ali, A., Pakula, H., Ashton, G., Peset, I., Brown, M., Clarke, N.W., et al. (2018). Single-cell analysis identifies LY6D as a marker linking castration-resistant prostate luminal cells to prostate progenitors and cancer. Cell Rep. *25*, 3504–3518.e6. https://doi.org/10.1016/j.celrep.2018.11.069.

7. Choi, N., Zhang, B., Zhang, L., Ittmann, M., and Xin, L. (2012). Adult murine prostate basal and luminal cells are self-sustained lineages that can both serve as targets for prostate cancer initiation. Cancer Cell *21*, 253–265. https://doi.org/10.1016/j.ccr.2012.01.005.

8. Crowley, L., Cambuli, F., Aparicio, L., Shibata, M., Robinson, B.D., Xuan, S., Li, W., Hibshoosh, H., Loda, M., Rabadan, R., and Shen, M.M. (2020). A single-cell atlas of the mouse and human prostate reveals heterogeneity and conservation of epithelial progenitors. Elife *9*, e59465. https://doi.org/10.7554/elife.59465.

9. Guo, W., Li, L., He, J., Liu, Z., Han, M., Li, F., Xia, X., Zhang, X., Zhu, Y., Wei, Y., et al. (2020). Single-cell transcriptomics identifies a distinct luminal progenitor cell type in distal prostate invagination tips. Nat. Genet. *52*, 908–918. https://doi.org/10.1038/s41588-020-0642-1.

10. Karthaus, W.R., Iaquinta, P.J., Drost, J., Gracanin, A., van Boxtel, R., Wongvipat, J., Dowling, C.M., Gao, D., Begthel, H., Sachs, N., et al. (2014). Identification of multipotent luminal progenitor cells in human prostate organoid cultures. Cell *159*, 163–175. https://doi.org/10.1016/j.cell.2014.08.017.

11. Karthaus, W.R., Hofree, M., Choi, D., Linton, E.L., Turkekul, M., Bejnood, A., Carver, B., Gopalan, A., Abida, W., Laudone, V., et al. (2020). Regenerative potential of prostate luminal cells revealed by single-cell analysis. Science *368*, 497–505. https://doi.org/10.1126/science.aay0267.

12. Mevel, R., Steiner, I., Mason, S., Galbraith, L.C., Patel, R., Fadlullah, M.Z., Ahmad, I., Leung, H.Y., Oliveira, P., Blyth, K., et al. (2020). RUNX1 marks a luminal castration-resistant lineage established at the onset of prostate development. Elife *9*, e60225. https://doi.org/10.7554/elife.60225.

13. Ousset, M., Van Keymeulen, A., Bouvencourt, G., Sharma, N., Achouri, Y., Simons, B.D., and Blanpain, C. (2012). Multipotent and unipotent progenitors contribute to prostate postnatal development. Nat. Cell Biol. *14*, 1131–1138. https://doi.org/10.1038/ncb2600.

14. Wang, Z.A., Mitrofanova, A., Bergren, S.K., Abate-Shen, C., Cardiff, R.D., Califano, A., and Shen, M.M. (2013). Lineage analysis of basal epithelial cells reveals their unexpected plasticity and supports a cell-of-origin model for prostate cancer heterogeneity. Nat. Cell Biol. *15*, 274–283. https://doi.org/10.1038/ncb2697.

15. Henry, G.H., Malewska, A., Joseph, D.B., Malladi, V.S., Lee, J., Torrealba, J., Mauck, R.J., Gahan, J.C., Raj, G.V., Roehrborn, C.G., et al. (2018). A cellular anatomy of the normal adult human prostate and prostatic urethra. Cell Rep. *25*, 3530–3542.e5. https://doi.org/10.1016/j.celrep.2018.11.086.

16. Joseph, D.B., Henry, G.H., Malewska, A., Iqbal, N.S., Ruetten, H.M., Turco, A.E., Abler, L.L., Sandhu, S.K., Cadena, M.T., Malladi, V.S., et al. (2020). Urethral luminal epithelia are castration-insensitive cells of the proximal prostate. Prostate *80*, 872–884. https://doi.org/10.1002/pros.24020.

17. Cancer Genome Atlas Research Network, Abeshouse, A., Ahn, J., Akbani, R., Ally, A., Amin, S., Andry, C.D., Annala, M., Aprikian, A., Armenia, J., et al. (2015). The molecular taxonomy of primary prostate cancer. Cell *163*, 1011–1025. https://doi.org/10.1016/j.cell.2015.10.025.

18. Fraser, M., Sabelnykova, V.Y., Yamaguchi, T.N., Heisler, L.E., Livingstone, J., Huang, V., Shiah, Y.-J., Yousif, F., Lin, X., Masella, A.P., et al. (2017). Genomic hallmarks of localized, non-indolent prostate cancer. Nature *541*, 359–364. https://doi.org/10.1038/nature20788.

19. Gundem, G., Van Loo, P., Kremeyer, B., Alexandrov, L.B., Tubio, J.M.C., Papaemmanuil, E., Brewer, D.S., Kallio, H.M.L., Högnäs, G., Annala, M., et al. (2015). The evolutionary history of lethal metastatic prostate cancer. Nature *520*, 353–357. https://doi.org/10.1038/nature14347.

20. Quigley, D.A., Dang, H.X., Zhao, S.G., Lloyd, P., Aggarwal, R., Alumkal, J.J., Foye, A., Kothari, V., Perry, M.D., Bailey, A.M., et al. (2018). Genomic hallmarks and structural variation in metastatic prostate cancer. Cell *174*, 758–769.e9. https://doi.org/10.1016/j.cell.2018.06.039.

21. Robinson, D., Van Allen, E.M., Wu, Y.-M., Schultz, N., Lonigro, R.J., Mosquera, J.-M., Montgomery, B., Taplin, M.-E., Pritchard, C.C., Attard, G., et al. (2015). Integrative clinical genomics of advanced prostate cancer. Cell *161*, 1215–1228. https://doi.org/10.1016/j.cell.2015.05.001.

22. Jamaspishvili, T., Berman, D.M., Ross, A.E., Scher, H.I., De Marzo, A.M., Squire, J.A., and Lotan, T.L. (2018). Clinical implications of PTEN loss in prostate cancer. Nat. Rev. Urol. *15*, 222–234. https://doi.org/10.1038/nrurol.2018.9.

23. Song, M.S., Salmena, L., and Pandolfi, P.P. (2012). The functions and regulation of the PTEN tumour suppressor. Nat. Rev. Mol. Cell Biol. *13*, 283–296. https://doi.org/10.1038/nrm3330.

24. Wang, X., Kruithof-de Julio, M., Economides, K.D., Walker, D., Yu, H., Halili, M.V., Hu, Y.-P., Price, S.M., Abate-Shen, C., and Shen, M.M. (2009). A luminal epithelial stem cell that is a cell of origin for prostate cancer. Nature *461*, 495–500. https://doi.org/10.1038/nature08361.

25. Xie, Q., Liu, Y., Cai, T., Horton, C., Stefanson, J., and Wang, Z.A. (2017). Dissecting cell-type-specific roles of androgen receptor in prostate homeostasis and regeneration through lineage tracing. Nat. Commun. *8*, 14284. https://doi.org/10.1038/ncomms14284.

26. Lu, T.-L., Huang, Y.-F., You, L.-R., Chao, N.-C., Su, F.-Y., Chang, J.-L., and Chen, C.-M. (2013). Conditionally ablated pten in prostate basal cells promotes basal-to-luminal differentiation and causes invasive prostate cancer in mice. Am. J. Pathol. *182*, 975–991. https://doi.org/10.1016/j.ajpath.2012.11.025.

27. Ghosh, S., Varela, L., Sood, A., Park, B.H., and Lotan, T.L. (2013). mTOR signaling feedback modulates mammary epithelial differentiation and restrains invasion downstream of PTEN loss. Cancer Res. *73*, 5218–5231. https://doi.org/10.1158/0008-5472.can-13-0429.

28. Park, J.W., Lee, J.K., Phillips, J.W., Huang, P., Cheng, D., Huang, J., and Witte, O.N. (2016). Prostate epithelial cell of origin determines cancer

differentiation state in an organoid transformation assay. Proc. Natl. Acad. Sci. USA *113*, 4482–4487. https://doi.org/10.1073/pnas.1603645113.

29. Sun, Y., Wang, B.-E., Leong, K.G., Yue, P., Li, L., Jhunjhunwala, S., Chen, D., Seo, K., Modrusan, Z., Gao, W.-Q., et al. (2012). Androgen deprivation causes epithelial–mesenchymal transition in the prostate: implications for androgen-deprivation therapy. Cancer Res. *72*, 527–536. https://doi.org/10.1158/0008-5472.can-11-3004.

30. Ye, X., Tam, W.L., Shibue, T., Kaygusuz, Y., Reinhardt, F., Ng Eaton, E., and Weinberg, R.A. (2015). Distinct EMT programs control normal mammary stem cells and tumour-initiating cells. Nature *525*, 256–260. https://doi.org/10.1038/nature14897.

31. Bishop, J.L., Thaper, D., and Zoubeidi, A. (2014). The multifaceted roles of STAT3 signaling in the progression of prostate cancer. Cancers *6*, 829–859. https://doi.org/10.3390/cancers6020829.

32. Kassis, J., Moellinger, J., Lo, H., Greenberg, N.M., Kim, H.G., and Wells, A. (1999). A role for phospholipase C-gamma-mediated signaling in tumor cell invasion. Clin. Cancer Res. *5*, 2251–2260.

33. Ramsay, A.K., McCracken, S.R.C., Soofi, M., Fleming, J., Yu, A.X., Ahmad, I., Morland, R., Machesky, L., Nixon, C., Edwards, D.R., et al. (2011). ERK5 signalling in prostate cancer promotes an invasive phenotype. Br. J. Cancer *104*, 664–672. https://doi.org/10.1038/sj.bjc.6606062.

34. Freed, D.M., Bessman, N.J., Kiyatkin, A., Salazar-Cavazos, E., Byrne, P.O., Moore, J.O., Valley, C.C., Ferguson, K.M., Leahy, D.J., Lidke, D.S., and Lemmon, M.A. (2017). EGFR ligands differentially stabilize receptor dimers to specify signaling kinetics. Cell *171*, 683–695.e18. https://doi.org/10.1016/j.cell.2017.09.017.

35. Wilson, K.J., Mill, C., Lambert, S., Buchman, J., Wilson, T.R., Hernandez-Gordillo, V., Gallo, R.M., Ades, L.M.C., Settleman, J., and Riese, D.J. (2012). EGFR ligands exhibit functional differences in models of paracrine and autocrine signaling. Growth Factors *30*, 107–116. https://doi.org/10.3109/08977194.2011.649918.

36. Zuo, W.L., Yang, J., Gomi, K., Chao, I., Crystal, R.G., and Shaykhiev, R. (2017). EGF-Amphiregulin interplay in airway stem/progenitor cells links the pathogenesis of smoking-induced lesions in the human airway epithelium. Stem Cell. *35*, 824–837. https://doi.org/10.1002/stem.2512.

37. Jurmeister, S., Ramos-Montoya, A., Sandi, C., Pértega-Gomes, N., Wadhwa, K., Lamb, A.D., Dunning, M.J., Attig, J., Carroll, J.S., Fryer, L.G., et al. (2018). Identification of potential therapeutic targets in prostate cancer through a cross-species approach. EMBO Mol. Med. *10*, e8274. https://doi.org/10.15252/emmm.201708274.

38. Garcia-Alonso, L., Holland, C.H., Ibrahim, M.M., Turei, D., and Saez-Rodriguez, J. (2019). Benchmark and integration of resources for the estimation of human transcription factor activities. Genome Res. *29*, 1363–1375. https://doi.org/10.1101/gr.240663.118.

39. Holland, C.H., Szalai, B., and Saez-Rodriguez, J. (2020). Transfer of regulatory knowledge from human to mouse for functional genomics analysis. Biochim. Biophys. Acta. Gene Regul. Mech. *1863*, 194431. https://doi.org/10.1016/j.bbagrm.2019.194431.

40. Tamama, K., and Barbeau, D.J. (2012). Early growth response genes signaling supports strong paracrine capability of mesenchymal stem cells. Stem Cells Int. *2012*, 428403. https://doi.org/10.1155/2012/428403.

41. Xu, Q., Long, Q., Zhu, D., Fu, D., Zhang, B., Han, L., Qian, M., Guo, J., Xu, J., Cao, L., et al. (2019). Targeting amphiregulin (AREG) derived from senescent stromal cells diminishes cancer resistance and averts programmed cell death 1 ligand (PD-L1)-mediated immunosuppression. Aging Cell *18*, e13027. https://doi.org/10.1111/acel.13027.

42. Inui, S., Higashiyama, S., Hashimoto, K., Higashiyama, M., Yoshikawa, K., and Taniguchi, N. (1997). Possible role of coexpression of CD9 with membrane-anchored heparin-binding EGF-like growth factor and amphiregulin in cultured human keratinocyte growth. J. Cell. Physiol. *171*, 291–298. https://doi.org/10.1002/(sici)1097-4652(291)171:3<291::aid-jcp7>3.0.co;2-j.

43. Levano, K.S., and Kenny, P.A. (2012). Clarification of the C-terminal proteolytic processing site of human Amphiregulin. FEBS Lett. *586*, 3500–3502. https://doi.org/10.1016/j.febslet.2012.07.078.

44. Sahin, U., Weskamp, G., Kelly, K., Zhou, H.-M., Higashiyama, S., Peschon, J., Hartmann, D., Saftig, P., and Blobel, C.P. (2004). Distinct roles for ADAM10 and ADAM17 in ectodomain shedding of six EGFR ligands. J. Cell Biol. *164*, 769–779. https://doi.org/10.1083/jcb.200307137.

45. Shoyab, M., McDonald, V.L., Bradley, J.G., and Todaro, G.J. (1988). Amphiregulin: a bifunctional growth-modulating glycoprotein produced by the phorbol 12-myristate 13-acetate-treated human breast adenocarcinoma cell line MCF-7. Proc. Natl. Acad. Sci. USA *85*, 6528–6532. https://doi.org/10.1073/pnas.85.17.6528.

46. Keates, S., Han, X., Kelly, C.P., and Keates, A.C. (2007). Macrophage-inflammatory protein-3α mediates epidermal growth factor receptor transactivation and ERK1/2 MAPK signaling in caco-2 colonic epithelial cells via metalloproteinase-dependent release of amphiregulin. J. Immunol. *178*, 8013–8021. https://doi.org/10.4049/jimmunol.178.12.8013.

47. Sternlicht, M.D., Sunnarborg, S.W., Kouros-Mehr, H., Yu, Y., Lee, D.C., and Werb, Z. (2005). Mammary ductal morphogenesis requires paracrine activation of stromal EGFR via ADAM17-dependent shedding of epithelial amphiregulin. Development *132*, 3923–3933. https://doi.org/10.1242/dev.01966.

48. Isokane, M., Hieda, M., Hirakawa, S., Shudou, M., Nakashiro, K., Hashimoto, K., Hamakawa, H., and Higashiyama, S. (2008). Plasma-membrane-anchored growth factor pro-amphiregulin binds A-type lamin and regulates global transcription. J. Cell Sci. *121*, 3608–3618. https://doi.org/10.1242/jcs.031443.

49. Yoshida, M., Shimura, T., Fukuda, S., Mizoshita, T., Tanida, S., Kataoka, H., Kamiya, T., Nakazawa, T., Higashiyama, S., and Joh, T. (2012). Nuclear translocation of pro-amphiregulin induces chemoresistance in gastric cancer. Cancer Sci. *103*, 708–715. https://doi.org/10.1111/j.1349-7006.2012.02204.x.

50. Drost, J., Karthaus, W.R., Gao, D., Driehuis, E., Sawyers, C.L., Chen, Y., and Clevers, H. (2016). Organoid culture systems for prostate epithelial tissue and prostate cancer tissue. Nat. Protoc. *11*, 347–358. https://doi.org/10.1038/nprot.2016.006.

51. Haughey, C.M., Mukherjee, D., Steele, R.E., Popple, A., Dura-Perez, L., Pickard, A., Patel, M., Jain, S., Mullan, P.B., Williams, R., et al. (2020). Investigating radiotherapy response in a novel syngeneic model of prostate cancer. Cancers *12*, 2804. https://doi.org/10.3390/cancers12102804.

52. Crowell, P.D., Fox, J.J., Hashimoto, T., Diaz, J.A., Navarro, H.I., Henry, G.H., Feldmar, B.A., Lowe, M.G., Garcia, A.J., Wu, Y.E., et al. (2019). Expansion of luminal progenitor cells in the aging mouse and human prostate. Cell Rep. *28*, 1499–1510.e6. https://doi.org/10.1016/j.celrep.2019.07.007.

53. Kwon, O.J., Zhang, L., and Xin, L. (2016). Stem cell antigen-1 identifies a distinct androgen-independent murine prostatic luminal cell lineage with bipotent potential. Stem Cell. *34*, 191–202. https://doi.org/10.1002/stem.2217.

54. Yoo, Y.A., Roh, M., Naseem, A.F., Lysy, B., Desouki, M.M., Unno, K., and Abdulkadir, S.A. (2016). Bmi1 marks distinct castration-resistant luminal progenitor cells competent for prostate regeneration and tumour initiation. Nat. Commun. *7*, 12943. https://doi.org/10.1038/ncomms12943.

55. Grossmann, S., Hooks, Y., Wilson, L., Moore, L., O'Neill, L., Martincorena, I., Voet, T., Stratton, M.R., Heer, R., and Campbell, P.J. (2021). Development, maturation, and maintenance of human prostate inferred from somatic mutations. Cell Stem Cell *28*, 1262–1274.e5. https://doi.org/10.1016/j.stem.2021.02.005.

56. Abud, H.E., Chan, W.H., and Jardé, T. (2021). Source and impact of the EGF family of ligands on intestinal stem cells. Front. Cell Dev. Biol. *9*, 685665. https://doi.org/10.3389/fcell.2021.685665.

57. Ciarloni, L., Mallepell, S., and Brisken, C. (2007). Amphiregulin is an essential mediator of estrogen receptor α function in mammary gland

development. Proc. Natl. Acad. Sci. USA *104*, 5455–5460. https://doi.org/10.1073/pnas.0611647104.

58. Lindzen, M., Ghosh, S., Noronha, A., Drago, D., Nataraj, N.B., Leitner, O., Carvalho, S., Zmora, E., Sapoznik, S., Shany, K.B., et al. (2021). Targeting autocrine amphiregulin robustly and reproducibly inhibits ovarian cancer in a syngeneic model: roles for wildtype p53. Oncogene *40*, 3665–3679. https://doi.org/10.1038/s41388-021-01784-8.

59. Craft, N., Shostak, Y., Carey, M., and Sawyers, C.L. (1999). A mechanism for hormone-independent prostate cancer through modulation of androgen receptor signaling by the HER-2/neu tyrosine kinase. Nat. Med. *5*, 280–285. https://doi.org/10.1038/6495.

60. Yeh, S., Lin, H.-K., Kang, H.-Y., Thin, T.H., Lin, M.-F., and Chang, C. (1999). From HER2/Neu signal cascade to androgen receptor and its co-activators: a novel pathway by induction of androgen target genes through MAP kinase in prostate cancer cells. Proc. Natl. Acad. Sci. USA *96*, 5458–5463. https://doi.org/10.1073/pnas.96.10.5458.

61. Bostwick, D.G., Qian, J., and Maihle, N.J. (2004). Amphiregulin expression in prostatic intraepithelial neoplasia and adenocarcinoma: a study of 93 cases. Prostate *58*, 164–168. https://doi.org/10.1002/pros.10322.

62. Tørring, N., Hansen, F.D., Sørensen, B.S., Ørntoft, T.F., and Nexø, E. (2005). Increase in amphiregulin and epiregulin in prostate cancer xenograft after androgen deprivation—impact of specific HER1 inhibition. Prostate *64*, 1–8. https://doi.org/10.1002/pros.20214.

63. Davies, A.E., Pargett, M., Siebert, S., Gillies, T.E., Choi, Y., Tobin, S.J., Ram, A.R., Murthy, V., Juliano, C., Quon, G., et al. (2020). Systems-level properties of EGFR-RAS-ERK signaling amplify local signals to generate dynamic gene expression heterogeneity. Cell Syst. *11*, 161–175.e5. https://doi.org/10.1016/j.cels.2020.07.004.

64. Stoll, S.W., Johnson, J.L., Li, Y., Rittié, L., and Elder, J.T. (2010). Amphiregulin carboxy-terminal domain is required for autocrine keratinocyte growth. J. Invest. Dermatol. *130*, 2031–2040. https://doi.org/10.1038/jid.2010.98.

65. Gitenay, D., and Baron, V.T. (2009). Is EGR1 a potential target for prostate cancer therapy? Future Oncol. *5*, 993–1003. https://doi.org/10.2217/fon.09.67.

66. Li, L., Ameri, A.H., Wang, S., Jansson, K.H., Casey, O.M., Yang, Q., Beshiri, M.L., Fang, L., Lake, R.G., Agarwal, S., et al. (2019). EGR1 regulates angiogenic and osteoclastogenic factors in prostate cancer and promotes metastasis. Oncogene *38*, 6241–6255. https://doi.org/10.1038/s41388-019-0873-8.

67. Sauer, L., Gitenay, D., Vo, C., and Baron, V.T. (2010). Mutant p53 initiates a feedback loop that involves Egr-1/EGF receptor/ERK in prostate cancer cells. Oncogene *29*, 2628–2637. https://doi.org/10.1038/onc.2010.24.

68. Carver, B.S., Chapinski, C., Wongvipat, J., Hieronymus, H., Chen, Y., Chandarlapaty, S., Arora, V.K., Le, C., Koutcher, J., Scher, H., et al. (2011). Reciprocal feedback regulation of PI3K and androgen receptor signaling in PTEN-deficient prostate cancer. Cancer Cell *19*, 575–586. https://doi.org/10.1016/j.ccr.2011.04.008.

69. Sweeney, C., Bracarda, S., Sternberg, C.N., Chi, K.N., Olmos, D., Sandhu, S., Massard, C., Matsubara, N., Alekseev, B., Parnis, F., et al. (2021). Ipatasertib plus abiraterone and prednisolone in metastatic castration-resistant prostate cancer (IPATential150): a multicentre, randomised, double-blind, phase 3 trial. Lancet *398*, 131–142. https://doi.org/10.1016/s0140-6736(21)00580-8.

70. Braicu, C., Buse, M., Busuioc, C., Drula, R., Gulei, D., Raduly, L., Rusu, A., Irimie, A., Atanasov, A.G., Slaby, O., et al. (2019). A comprehensive Review on MAPK: a promising therapeutic target in cancer. Cancers *11*, 1618. https://doi.org/10.3390/cancers11101618.

71. Guérin, O., Fischel, J.L., Ferrero, J.-M., Bozec, A., and Milano, G. (2010). EGFR targeting in hormone-refractory prostate cancer: current appraisal and prospects for treatment. Pharmaceuticals *3*, 2238–2247. https://doi.org/10.3390/ph3072238.

72. Nastały, P., Stoupiec, S., Popęda, M., Smentoch, J., Schlomm, T., Morrissey, C., Żaczek, A.J., Beyer, B., Tennstedt, P., Graefen, M., et al. (2020). EGFR as a stable marker of prostate cancer dissemination to bones. Br. J. Cancer *123*, 1767–1774. https://doi.org/10.1038/s41416-020-01052-8.

73. Gross, M., Higano, C., Pantuck, A., Castellanos, O., Green, E., Nguyen, K., and Agus, D.B. (2007). A phase II trial of docetaxel and erlotinib as first-line therapy for elderly patients with androgen-independent prostate cancer. BMC Cancer *7*, 142. https://doi.org/10.1186/1471-2407-7-142.

74. Nabhan, C., Lestingi, T.M., Galvez, A., Tolzien, K., Kelby, S.K., Tsarwhas, D., Newman, S., and Bitran, J.D. (2009). Erlotinib has moderate single-agent activity in chemotherapy-naïve castration-resistant prostate cancer: final results of a phase II trial. Urology *74*, 665–671. https://doi.org/10.1016/j.urology.2009.05.016.

75. Pezaro, C., Rosenthal, M.A., Gurney, H., Davis, I.D., Underhill, C., Boyer, M.J., Kotasek, D., Solomon, B., and Toner, G.C. (2009). An open-label, single-arm phase two trial of gefitinib in patients with advanced or metastatic castration-resistant prostate cancer. Am. J. Clin. Oncol. *32*, 338–341. https://doi.org/10.1097/coc.0b013e31818b946b.

76. Salzberg, M., Rochlitz, C., Morant, R., Thalmann, G., Pedrazzini, A., Roggero, E., Schönenberger, A., Knuth, A., and Borner, M. (2007). An open-label, noncomparative phase II trial to evaluate the efficacy and safety of docetaxel in combination with gefitinib in patients with hormone-refractory metastatic prostate cancer. Onkologie *30*, 355–360. https://doi.org/10.1159/000102452.

77. Small, E.J., Fontana, J., Tannir, N., DiPaola, R.S., Wilding, G., Rubin, M., Iacona, R.B., and Kabbinavar, F.F. (2007). A phase II trial of gefitinib in patients with non-metastatic hormone-refractory prostate cancer. BJU Int. *100*, 765–769. https://doi.org/10.1111/j.1464-410x.2007.07121.x.

78. Sridhar, S.S., Hotte, S.J., Chin, J.L., Hudes, G.R., Gregg, R., Trachtenberg, J., Wang, L., Tran-Thanh, D., Pham, N.-A., Tsao, M.-S., et al. (2010). A multicenter phase II clinical trial of lapatinib (GW572016) in hormonally untreated advanced prostate cancer. Am. J. Clin. Oncol. *33*, 609–613. https://doi.org/10.1097/coc.0b013e3181beac33.

79. Whang, Y.E., Armstrong, A.J., Rathmell, W.K., Godley, P.A., Kim, W.Y., Pruthi, R.S., Wallen, E.M., Crane, J.M., Moore, D.T., Grigson, G., et al. (2013). A phase II study of lapatinib, a dual EGFR and HER-2 tyrosine kinase inhibitor, in patients with castration-resistant prostate cancer. Urol. Oncol. *31*, 82–86. https://doi.org/10.1016/j.urolonc.2010.09.018.

80. Nickols, N.G., Nazarian, R., Zhao, S.G., Tan, V., Uzunangelov, V., Xia, Z., Baertsch, R., Neeman, E., Gao, A.C., Thomas, G.V., et al. (2019). MEK-ERK signaling is a therapeutic target in metastatic castration resistant prostate cancer. Prostate Cancer Prostatic Dis. *22*, 531–538. https://doi.org/10.1038/s41391-019-0134-5.

81. Fuerer, C., and Nusse, R. (2010). Lentiviral vectors to Probe and manipulate the wnt signaling pathway. PLoS One *5*, e9370. https://doi.org/10.1371/journal.pone.0009370.

82. Baena, E., Shao, Z., Linn, D.E., Glass, K., Hamblen, M.J., Fujiwara, Y., Kim, J., Nguyen, M., Zhang, X., Godinho, F.J., Bronson, R.T., Mucci, L.A., Loda, M., Yuan, G.C., Orkin, S.H., and Li, Z. (2013). ETV1 directs androgen metabolism and confers aggressice prostate cancer in targeted mice and patients. Genes Dev *27*, 683–698. https://doi.org/10.1101/gad.211011.112.

83. Robinson, M.D., McCarthy, D.J., and Smyth, G.K. (2010). edgeR: a Bioconductor package for differential expression analysis of digital gene expression data. Bioinformatics *26*, 139–140. https://doi.org/10.1093/bioinformatics/btp616.

84. Bankhead, P., QuPath, et al. (2017). Open source software for digital pathology image analysis. Scientific Reports. https://doi.org/10.1038/s41598-017.

85. Dobin, A., et al. (2013). STAR: ultrafast universal RNA-seq aligner. Bioinformatics *29*, 15–21. https://doi.org/10.1093/bioinformatics/bts635.

86. Schindelin, J., Arganda-Carreras, I., Frise, E., et al. (2012). Fiji: an open-source platform for biological-image analysis. Nat Methods *9*, 676–682. https://doi.org/10.1038/nmeth.2019.

87. Gearing, L.J., Cumming, H.E., Chapman, R., Finkel, A.M., Woodhouse, I.B., Luu, K., et al. (2019). CiiiDER: A tool for predicting and analysing transcription factor binding sites. PLoS ONE *14*, e0215495. https://doi.org/10.1371/journal.pone.0215495.

88. Xavier, M. (2002). et al.PROMO:detection of known transcription regulatory elements using species-tailored searches. Bioinformatics *18*, 333–334. https://doi.org/10.1093/bioinformatics/18.2.333.

89. Srinivas, S., Watanabe, T., Lin, C.-S., William, C.M., Tanabe, Y., Jessell, T.M., and Costantini, F. (2001). Cre reporter strains produced by targeted insertion of EYFP and ECFP into the ROSA26 locus. BMC Dev. Biol. *1*, 4. https://doi.org/10.1186/1471-213x-1-4.

90. Van Keymeulen, A., Rocha, A.S., Ousset, M., Beck, B., Bouvencourt, G., Rock, J., Sharma, N., Dekoninck, S., and Blanpain, C. (2011). Distinct stem cells contribute to mammary gland development and maintenance. Nature *479*, 189–193. https://doi.org/10.1038/nature10573.

91. Lesche, R., Groszer, M., Gao, J., Wang, Y., Messing, A., Sun, H., Liu, X., and Wu, H. (2002). Cre/loxP-mediated inactivation of the murine Pten tumor suppressor gene. Genesis *32*, 148–149. https://doi.org/10.1002/gene.10036.

92. Mootha, V.K., Lindgren, C.M., Eriksson, K.-F., Subramanian, A., Sihag, S., Lehar, J., Puigserver, P., Carlsson, E., Ridderstråle, M., Laurila, E., et al. (2003). PGC-1α-responsive genes involved in oxidative phosphorylation are coordinately downregulated in human diabetes. Nat. Genet. *34*, 267–273. https://doi.org/10.1038/ng1180.

93. Subramanian, A., Tamayo, P., Mootha, V.K., Mukherjee, S., Ebert, B.L., Gillette, M.A., Paulovich, A., Pomeroy, S.L., Golub, T.R., Lander, E.S., and Mesirov, J.P. (2005). Gene set enrichment analysis: a knowledge-based approach for interpreting genome-wide expression profiles. Proc. Natl. Acad. Sci. USA *102*, 15545–15550. https://doi.org/10.1073/pnas.0506580102.

STAR★METHODS

KEY RESOURCES TABLE

REAGENT or RESOURCE	SOURCE	IDENTIFIER
Antibodies		
Rabbit monoclonal anti-phospho-AKT (Ser473)	Cell Signaling Technology	3787S; RRID: AB_331170
Rabbit monoclonal anti-GFP	Cell Signaling Technology	2956; RRID:AB_1196615
Rabbit monoclonal anti-Cytokeratin 8 (K8)	Abcam	ab53280; RRID:AB_869901
Rabbit monoclonal anti-Cytokeratin 5 (K5)	Abcam	ab52635; RRID:AB_869890
Rabbit monoclonal anti-P63	Cell Signaling Technology	39692; RRID:AB_2799159
Rabbit monoclonal anti-AR	Abcam	ab133273; RRID:AB_11156085
Rabbit monoclonal anti-PTEN	Cell Signaling Technology	9188; RRID:AB_2253290
Rabbit polyclonal anti-LY6D	Proteintech	17361-1-AP; RRID:AB_2878397
Goat polyclonal anti-AREG	R&D	AF989; RRID:AB_2060663
Rabbit polyclonal anti-LY6D	Sigma-Aldrich	HPA 024755; RRID:AB_1853410
Rabbit monoclonal anti-PSMA	Abcam	ab133579; RRID:AB_1310623
Mouse monoclonal anti-Pan-Cytokeratin	Sigma-Aldrich	C2931; RRID:AB_258824
Rat monoclonal anti-EpCAM-APC	ebioscience	17–5791; RRID:AB_1659714
Rat monoclonal anti-LY6D-PE	ebioscience	12–5974; RRID:AB_11042719
Rat monoclonal anti-CD49f-FITC	Biolegend	313606; RRID:AB_345300
Rat monoclonal anti-CD24- BV786	BD Biosciences	744470; RRID:AB_2742258
Rabbit polyclonal Anti-EGFR	Sigma-Aldrich	HPA018530; RRID:AB_1848044
Rabbit polyclonal Anti-phospho-EGFR, (Tyr1086)	Invitrogen	36–9700; RRID:AB_2533287
Rabbit polyclonal Anti-phospho-EGFR, (Tyr992)	Cell Signaling Technology	2235; RRID:AB_331708
Rabbit polyclonal Anti-phospho-EGFR, (Tyr845)	Invitrogen	44-784G; RRID:AB_1500036
Rabbit Monoclonal Anti-phospho-PLCG1 (Tyr783)	Invitrogen	700044; RRID:AB_2532275
Rabbit monoclonal Anti-MAPK p44/42, Erk1/2	Cell Signaling Technology	4695; RRID:AB_390779
Rabbit polyclonal Anti-phospho-MAPK p44/42, Erk1/2 (Thr202/Tyr204)	Cell Signaling Technology	9101; RRID:AB_331646
Rabbit monoclonal Anti-AKT	Cell Signaling Technology	4691; RRID:AB_915783
Rabbit monoclonal Anti-phospho-AKT, (Ser473)	Cell Signaling Technology	4060S; RRID:AB_2315049
Rabbit monoclonal Anti-EGR1	ThermoFisher Scientific	MA5-15009; RRID:AB_10982091
Mouse monoclonal Anti-VINCULIN	Sigma-Aldrich	V4505; RRID:AB_477617
Rat monoclonal Anti-LY6D (FITC-conjugated), clone 49-H4	BioLegend	138605; RRID:AB_11203901
Rabbit polyclonal Anti-AREG	Affinity Biosciences	DF6665; RRID:AB_2838627
Goat polyclonal Anti-AREG	R&D systems	AF262; RRID:AB_2243124
IgG rabbit isotype control	Santa Cruz Biotechnology	sc-2027; RRID:AB_737197
Anti-rabbit secondary antibody, Alexa Fluor 594	Thermo Fisher	A-11037; RRID:AB_2534095
Anti-mouse HRP-conjugated secondary antibody	Cell Signaling Technology	7076S; RRID:AB_330924

(*Continued on next page*)

Continued

REAGENT or RESOURCE	SOURCE	IDENTIFIER
Anti-rabbit HRP-conjugated secondary antibody	Santa Cruz Biotechnology	sc-2004; RRID:AB_631746
IgG goat isotype control	ThermoFisher	31245; RRID:AB_10959406
Rat monoclonal Anti-LY6D, clone 49-H4	BD Biosciences	561147; RRID:AB_10563420
IgG rabbit isotype control	ThermoFisher	AF568; RRID:AB_243593
Biological samples		
FFPE human prostate tissue microarray	Manchester Cancer Research Center Biobank	MCRC Biobank: 16_RIMA_06
FFPE human prostate tissue biopsy specimens	Manchester Cancer Research Center Biobank	IRAS project ID: 211571
Chemicals, peptides, and recombinant proteins		
BOND Epitope Retrieval Solution 1	Leica Biosystems	AR9961
BOND Epitope Retrieval Solution 2	Leica Biosystems	AR9640
Casein blocking solution	Vector labs	SP-5020
Opal Automation IHC kit	Akoya	NEL821001KT
RNAscope® 2.5 LS Probe - Mm-*Ly6d*	ACD	532078
ProLong Gold Antifade Mountant	Thermo Fisher	P10144
DAPI	Sigma-Aldrich	D9542
Paraformaldehyde	Polysciences	18814
Penicillin/Streptomycin (100x)	Thermo Fisher Scientific	15140122
Glutamax (100x)	Thermo Fisher Scientific	35050061
HEPES (1 M)	Thermo Fisher Scientific	15630080
B27 (50x)	Thermo Fisher Scientific	17504044
Human EGF	Peprotech	AF-100-15
R-Spondin1 Conditioned medium	Prepared in the laboratory	N/A
Mouse Noggin	Peprotech	250–38
ROCK inhibitor (Y-27632)	Sigma-Aldrich	Y0503-1MG
A83-01	Tocris Bioscience	2939
5α-Dihydrotestosterone (DHT)	Sigma-Aldrich	730637
N-acetylcysteine	Sigma-Aldrich	A9165
BME Type 2	Cultrex	3533-005-02
ADMEM/F12	Thermo Fisher Scientific	11330032
Tryple	Life Technologies	12563011
Penicillin-Streptomycin-Glutamine	Life Technologies	10378016
Dispase II	Gibco	17105041
Fetal Bovine Serum (FBS)	Sigma	F7524
SYBR Safe	Invitrogen	10328162
MyTaq Red mix	Bioline	BIO-25043
Tamoxifen	Sigma	T5648
Sunflower oil	Sigma	S5007
EnVision+/HRP mouse	Agilent	K400111-2
EnVision+/HRP rabbit	Agilent	K400311-2
Trametenib	Selleckchem	S2673
Erlotinib	Selleckchem	S1023
DharmaFECT 3 Transfection reagent	Dharmacon	T-2003-01
Recombinant mouse AREG protein	R&D Systems	989-AR-100
Recombinant R-spondin 1 protein	Peprotech	315–32
RPMI 1640 medium	Sigma	R7509
RIPA Lysis Buffer (10x)	Abcam	ab156034

(*Continued on next page*)

Continued

REAGENT or RESOURCE	SOURCE	IDENTIFIER
Pierce™ ECL Plus Western Blotting Substrate	Life Technologies	32132
DMSO	Sigma-Aldrich	276855
Immun-Blot® PVDF Membrane	BIO-RAD	1620177
Restore™ Plus Western Blot Stripping Buffer	Thermo Scientific	46430
Hanks Balanced Salt Solution	Gibco	14170112
EDTA (0.5 m), pH 8.0	Thermo Scientific	AM9261
FastStart Essential DNA Green Master	Roche	06402712001
PhosSTOP™, tablets	Roche	4906837001
Trypsin 0.25%	Sigma-Aldrich	25200056
Complete Ultra Tablets, Mini, EASYpack Protease Inhibitor Cocktail Tablets	Roche	5892970001
Cultrex Organoid Harvesting Solution	AMS Biotechnology (Europe) Limited	3700-100-01
Trametinib	Chemietek	CT-GSK212
Hydroxypropyl methyl cellulose (HPMC)	Sigma	09963
Tween 80	Sigma	P1754
Critical commercial assays		
RNA/DNA Purification Micro Kit	Norgen	50300
Superscript II	Thermo Fisher	18064022
Kapa Hifi Hotstart Readymix PCR kit	Roche	KR0370
Nextera XT DNA Library Preparation Kit	Illumina	FC-131-1024
Kapa Library Quantification Kit	Roche	07960336001
Pierce BCA Protein Assay Kit	Thermo Fisher Scientific	23225
Mouse Amphiregulin DuoSet ELISA Kit	R&D	DY989
RNeasy Plus Mini Kit (50)	Qiagen	74134
4–20% Mini-PROTEAN® TGX™ Precast Protein Gels	BIO-RAD	4561096
ELISA DuoSEt 2 ®	R&D Systems	DY008
CELL TITER 96® Non-Radioactive Cell Proliferation Assay	Promega	G4002
iScript™ cDNA Synthesis Kit	Bio-Rad	1708891
RNA purification PureLink RNA MicroKit	Invitrogen	12183–016
High-Capacity cDNA Reverse Transcription Kit	Applied Biosystems	4368814
SYBR Green PCR Master Mix	Applied Biosystems	4309155
Deposited data		
Raw and analyzed mouse bulk mRNA sequencing data	This paper	GEO: GSE174383
RNA-seq gene expression data set	Xu, et al. (2019)[41]	GEO: GSE116864
RNA-seq gene expression data set	Jurmeister, et al. (2018)[37]	GEO: GSE94574
Experimental models: Cell lines		
Mouse: DVL3	Haughey, et al. (2020)[51]	N/A
HA-R-Spondin1 293T cell line	Cultrex	3710-001-K
HEK 293 7TFP WNT reporter cell line	Fuerer & Nusse, (2010)[81]	N/A
Experimental models: Organisms/strains		
K8-CreER^{T2};Pten$^{Flox/Flox}$;R26-EYFP (K8PY)	This paper	N/A
K8-CreER^{T2};Pten$^{+/+}$;R26-EYFP (K8Y)	This paper	N/A

(*Continued on next page*)

Continued

REAGENT or RESOURCE	SOURCE	IDENTIFIER
Rosa26-Stop$^{Flox/Flox}$-EYFP (R26-EYFP);*Pten$^{Flox/Flox}$*	Prof. Stuart Orkin's laboratory	N/A
Tg(Krt8-cre/ERT2)17Blpn/J (*K8-CreERT2*)	The Jackson Laboratory	017947
Oligonucleotides		
Pten genotyping F: CAAGCACTCT GCGAACTGAG	The Jackson Laboratory	Pten<tm1Hwu>, oIMR9554
Pten genotyping R: GCATTGTG CTCTTCACTCCA	Baena et al. (2013)[82]	N/A
Table S4 for more information on the primers used in this study	Sigma-Aldrich	N/A
Table S4 for more information on the siRNAs used in this study	GE Healthcare (Dharmacon)	N/A
Software and algorithms		
GraphPad Prism v9.0.0	GraphPad	https://www.graphpad.com/scientific-software/prism/
R v4.0.2	R Core Team (2020)	https://www.R-project.org/
Rstudio	Rstudio	https://rstudio.com/
DoRothEA	Holland et al. (2019)[38]	https://saezlab.github.io/dorothea/
FlowJo v10	BD Biosciences	www.flowjo.com
edgeR	Robinson et al. (2010)[83]	https://doi.org/10.18129/B9.bioc.edgeR
IPA (The Ingenuity Pathway Analysis)	Qiagen	https://digitalinsights.qiagen.com/
QuPath v0.2.3	Bankhead et al. (2017)[84]	https://qupath.github.io/
STAR aligner	Dobin et al. (2012)[85]	https://doi.org/10.1093/bioinformatics/bts635
Harmony® 4.9 image analysis system	PerkinElmer	www.perkinelmer.com
ImageJ	NIH	https://imagej.nih.gov/ij/
Gene Set Enrichment Assay	GSEA	https://www.gsea-msigdb.org/gsea/index.jsp
FijI	Schindelin, et al. (2012)[86]	https://doi.org/10.1038/nmeth.2019
CiiiDER	Gearing, et al. (2019)[87]	https://doi.org/10.1371/journal.pone.0215495
PROMO Version 3.0.2	Xavier, et al. (2002)[88]	https://doi.org/10.1093/bioinformatics/18.2.333
Other		
Nextseq 500 sequencer	Illumina	SY-415-1001
Agilent 2100 Bioanalyzer	Agilent	G2939BA
Olympus VS.120 system	Olympus	www.olympus-lifescience.com
Olympus VS.200 system	Olympus	www.olympus-lifescience.com
Leica SCN400 Slide Scanner	Leica Biosystems	www.leicabiosystems.com
Opera Phenix™ High Content Screening System	PerkinElmer	www.perkinelmer.com
FACSAria III	BD Biosciences	www.bdbiosciences.com
ChemiDoc Imaging System	Bio-Rad	https://www.bio-rad.com/
LSM 880	Zeiss	
Roche Lightcycler 96	Roche	https://lifescience.roche.com

RESOURCE AVAILABILITY

Lead contact

Further information and requests for resources and reagents should be directed to and will be fulfilled by the lead contact, Esther Baena (esther.baena@cruk.manchester.ac.uk).

Materials availability

This study did not generate new unique reagents.

Data and code availability

- The datasets generated during this study have been deposited at Gene Expression Omnibus (GSE174383).
- This paper does not report original code.
- Any additional information required to reanalyze the data reported in this paper is available from the lead contact upon request.

EXPERIMENTAL MODEL AND SUBJECT DETAILS

Mice strains

Adult male mice (8-70 weeks-old) were used in this study in accordance with the PPL70/8580 and PP7381472 licenses approved by the Animal Welfare and Ethical Review Bodies (AWERB) of the CRUK Manchester Institute, and in accordance with National Home Office regulations under the Animals (Scientific Procedures) Act 1986. Lineage tracing *K8-CreER^{T2};Pten$^{Flox/Flox}$;R26-EYFP* (K8PY) and control *K8-CreER^{T2};Pten$^{+/+}$;R26-EYFP* (K8Y) genetically engineered mouse models (GEMM) were generated by introducing *Rosa26-Stop$^{Flox/Flox}$-EYFP* (R26EYFP) reporter mouse (C57BL/6)[89] to the *K8-CreER^{T2}*[90] and *Pten$^{FLox/Flox}$* line (C57BL/6).[91] The *R26EYFP and Pten$^{Flox/Flox}$* mice were kindly provided by Prof. Stuart Orkin's laboratory, and the *K8-CreER^{T2}* mice were obtained from The Jackson Laboratory. The mice lines were rederived at the Biological Research Unit at CRUK MI.

Murine cell lines

Murine DVL3 prostate cancer cells[51] were cultured in RPMI 1640 Phenol Red Free (Sigma, #R7509), supplemented with 10% fetal bovine serum (Sigma, #F7524), glutamine, penicillin, and streptomycin (Life Technologies, #10378016), meanwhile for experiments where starvation was necessary media was prepared without serum (blank RPMI media). All cell lines were maintained in a 5% CO_2 – controlled atmosphere at 37°C in a cell culture incubator.

Human tissue cohorts

Prostatectomy cohort

The POB prostate adenocarcinoma tissue micro array (TMA) and associated de-identified clinical information was constructed from the FFPE radical prostatectomy samples obtained from consented patients in collaboration with The Christie Hospital and the Manchester Cancer Research Center (MCRC) Biobank. This collection includes prostate tissue (tumor and normal) for 20 patients that underwent radical prostatectomy at The Christie Hospital. Specimens were selected from a cohort of intermediate to high-risk PCa patients (n = 20), of which 9 patients had localised disease without the nodal involvement (N0) and 11 patients presented with the pelvic LN invasion (N1) (Table S2). The H&E stained tissue sections were evaluated by the clinical pathologist Dr Pedro Oliveira, who selected the normal versus tumor tissue for the TMA build. At least 3 cores per tissue type (normal or tumor) per patient were selected. The cores were randomised throughout the 3 blocks. Dr Oliveira performed the Gleason scoring for each tumor area of the TMA cores.

ADT-treated cohort

Prostate cancer specimens were obtained from the AToM Clinical Study (Table S3) which is running at The Christie Hospital. PCa patients have received a standard diagnostic biopsy (Pre-ADT samples) followed by 6 months of ADT as per routine clinical practice (Post-ADT samples). The tissue specimens from consented patients were preserved in FFPE blocks.

METHOD DETAILS

Surgical castration

Male mice of at least 8 weeks of age were used for the surgery. Prior to the surgery, the animals were given analgesia Rymadyl (2 μL/g, in saline) subcutaneously in the scruff and were anesthetized using inhalation agent isolfurane (Teva) at 2.5–3% in 100% Oxygen. Buprecare (Buprenorphine) analgesia solution (0.05 μg/g, in saline) was additionally given subcutaneously in the scruff, before performing the invasive surgical procedures which are invading the body wall. All procedures were performed under surgically sterile conditions.

K8Y and K8PY experimental mice were castrated using standard techniques. Briefly, a small midline ventral incision was created in the skin. Epididymis was exposed and the testes, and the testes were removed by cauterisation. The remaining tissue was gently placed back under the skin and the technique was repeated on the other side. Skin incision was closed with the 6/0 absorbable surgical suture (Vicryl) in an interrupted pattern. The induction of Cre-recombinase was achieved by daily tamoxifen injections at least four weeks post-castration.

In vivo treatments

Tamoxifen treatment for the inducible Cre-driver mouse lines

Tamoxifen (#T5648, Sigma) was prepared as a 40 mg/mL solution in sunflower oil (#S5007, Sigma) with the addition of 96% ethanol (1:20 volume ratio). The solution was incubated at 55°C until the tamoxifen crystals were completely dissolved. Mice were treated with 100 μL of 40 mg/mL solution (4mg tamoxifen per ~30g of animal weight) per day and the solution was injected intraperitoneally (i.p.) into castrated (CR) or age-matched hormone-naive (HN) mice for 5 consecutive days. Mice were analyzed at selected timepoints (1-, 24- or 48 weeks post-tamoxifen induction). Fresh prostate tissue was isolated and immediately processed for single cells isolation or histological evaluation.

Trametinib (#CT-GSK212, Chemietek) was dissolved in a solution of 0.8% DMSO, 0.5% hydroxypropyl-methylcellulose, 0.2% Tween 80 and ddH2O at a concentration of 40 mg/mL. The suspended drug was administered daily into mice by oral gavage at 3 mL/kg (1mg Trametinib per kg mouse) for four weeks. Control mice received vehicle (DMSO:HPMC:T80:ddH2O) by oral gavage. Mice were analyzed after treatment. Fresh prostate tissue was isolated and immediately processed for histological evaluation.

Prostate single-cell isolation

Male mice were killed by Schedule 1 method at minimally 8 weeks of age by Schedule 1 procedure, and at specified timepoints post-tamoxifen treatment (1, 12, 24, 48 weeks). Murine prostate tissue was dissected as described previously.[50] Briefly, all urogenital system was collected, and ampullary gland was removed prior to the isolation of the prostate lobes. Lobes were dissected by carefully pulling proximal prostatic ducts from the urethra. Prostate tissue (all the lobes) was minced and digested in 1 mg/mL Collagenase I (#17018-029, Gibco) and 1 mg/mL Dispase II (#17105041, Gibco) dissolved in DMEM (#11965092, Gibco) + 5% FBS (#F7524, Sigma) + 1% Penicillin-Streptomycin-Glutamine (#10378016, Life Technologies). To prevent the anoikis, 10 μM ROCK inhibitor Y-27632 (#Y0503, Sigma) was added to the medium. Tissue was incubated for 1 h at 37°C with shaking. Cells were pelleted and washed with PBS. Then, the cells were incubated with Tryple (#12563011, Life Technologies) and 10 μM ROCK inhibitor for 5 min at 37°C. Warm media with 5% FBS was added to the cells to stop the enzymatic reaction and the cells were filtered through the 50 μm cell strainer. Single cells were pelleted and resuspended in 1 mL Advanced DMEM/F12 (#12634-010, ThermoFisher Scientific) with HEPES (#H0887, Sigma) and Glutamax (#35050061, Life Technologies). Single murine prostate cells were counted with the haemocytometer and were used fresh for organoid culture or were lysed for the DNA/RNA extraction.

Flow cytometry analysis

Dissociated single prostate cells were stained and sorted with BD FACS Aria II/III or Aria Fusion flow cytometer (Becton Dickinson). The following combination of cells surface markers were used to define the prostate cell populations: EpCAM, LY6D, CD49f, and CD24. The K8Y and K8PY mice endogenously express YFP upon tamoxifen treatment and live cells from these mice were selected by DAPI stain (Sigma-Aldrich, #D9542). FACS analysis (Figures 2 and S2) was performed using the FlowJo software (FlowJo 9).

Organoid-formation assay

Single cell suspension of murine prostate cells was sorted by the fluorescence-activated cell sorting (FACS). Sorted single cells were resuspended in 5 μL of blank ADMEM/F12 (Thermo Fisher Scientific, #11330032) medium with ROCK inhibitor (Y-27632), 5mM (Sigma-Aldrich, #Y0503-1MG), and embedded in 40μL of phenol red free Reduced growth factor matrix BME Type 2 (Cultrex, #3533-005-02L). Matrix-embedded cells were plated in the 96-well Optical-Bottom plates (PerkinElmer, #6055300), and incubated for 30 min at 37°C for the matrix to solidify. Murine prostate organoid culture medium (mPOM)[50] containing ADMEM/F12 (Thermo Fisher Scientific, #11330032) and supplements (Table S4) was added cells. Prostate cells were then incubated at 37°C, 5% CO2 for 7–10 days.

For the experiments where primary prostate organoids were treated with reduced growth factors media, EGF was excluded from the complete organoid culture media (rGF mPOM), and addition of amphiregulin (rGF mPOM + AREG, 100 ng/mL) or EGF (rGF mPOM + EGF, 50 ng/mL) indicated.

Production of R-Spondin 1 conditioned medium

The R-Spondin 1 conditioned media was produced using the HA-R-Spondin1 293T cell line (Cultrex, #3710-001-K), according to manufacturer's instructions (https://trevigen.com/). Each batch of R-Spondin 1 conditioned media was evaluated by the luciferase assay (Promega, #E4030) using the HEK 293 7TFP WNT reporter cell line,[81] and quantified by recombinant R-spondin1 (Peprotech, #315-32). Prostate organoid culture media was supplemented with 10% of the R-Spondin 1 conditioned media, which corresponds to the 500 ng/mL of the recombinant R-Spondin 1 protein.

Whole-mount immunostaining of organoids

After 7 days, organoids in the BME2 matrix were fixed in 4% paraformaldehyde (Polysciences, #18814) for 1h at room temperature (RT) and then gently washed three times in PBS. Permeabilization was performed using the 0.4% Triton X-100 in PBS (PBS-T) for 30 min, followed by incubation for 1 h in the blocking buffer (0.4% Triton X-100 + 2% FBS +1% BSA in PBS). Primary antibodies anti-mouse: LY6D (#49-H4, 1/100), Cytokeratin 8 (1/400), Cytokeratin 5 (1/100), p63 (1/800) were prepared in the blocking buffer at the optimised concentrations, and added to embedded organoid to incubate over-night at +4°C. Next day, the organoids were

washed three times for 1h each wash in PBS-T. Then, the samples were incubated with the secondary antibody (1/400) in blocking buffer for 2h at room temperature or over-night at +4°C. Organoids were washed three times for 1h each wash in PBS-T. The nuclear stain DAPI (Sigma-Aldrich, #D9542) was prepared in PBS-T, and organoids were incubated for 15–20 min on RT. The stained organoids were imaged on the confocal Opera Phenix High Content Screening System (PerkinElmer) and analyzed with the Harmony image analysis system (PerkinElmer).

Organoid imaging and image analysis

Phenotypic screening of live organoids in 96-well plates (PerkinElmer, #6055300) was performed using an Opera Phenix High Content Screening System (PerkinElmer). Confocal 10x imaging was used for the image acquisition in brightfield and YFP fluorescence channel. Acquired images were analyzed with the Harmony 4.9 image analysis system (PerkinElmer). Morphological features such as the mean surface area and roundness were calculated from the maximum intensity projection images in the YFP channel. Organoids were quantified as single clonal stem/progenitor cell outgrowth of >50 μm in diameter, in agreement with previous reports.[5,6]

ELISA and protein quantification

Sorted cell populations were seeded in organoid-growing conditions at 3000 cells per well (in the 96-well plate) in complete mPOM or under reduced growth factors (rGF mPOM). After 7 days of incubation at 37°C, media was removed and the organoid were washed twice with PBS. Blank AdDMEM media was added to the organoid culture for conditioning for 24 h at 37°C. Conditioned media was collected and analyzed by the Mouse Amphiregulin DuoSet ELISA Kit (R&D, DY989) according to the manufacturer's instructions. Organoids were dissociated for protein extraction and quantification (Pierce BCA Protein Assay Kit, Thermo Fisher Scientific, #23225). Four Parameter Logistic Regression model was applied for quantification and the results were normalised by the total protein concentration.

Evaluation of activation of EGFR/ERK pathway in DVL3 cells

0.5×10^6 DVL3 cells were cultivated in 6 well plate. After the cells were confluent, they were washed two times with PBS and then, serum starvation was made for 2 h before experiment in order to eliminate any growth factor included in complete media. Serum-starved cells were treated with 50 ng/mL human EGF (Peprotech, #AF-100-15) or 100 ng/mL recombinant mouse AREG (R&D systems, # 989-AR-100) respectively at different time points: 5-, 15- or 30-min. Stimulations were terminated by washing the cells once with PBS and then harvested by scraping them in RIPA buffer (Abcam, #ab156034) with protease inhibitors (Roche, #05892970001) and phosphatase inhibitors (Roche, #04906845001). Samples were incubated 10 min at 4°C and disrupted mechanically. Subsequently, samples were centrifugated at 13,000 × rpm for 20 min at 4°C, the supernatant were subjected to protein quantification, electrophoresis and immunoblotting.

Inhibition of phosphorylation of EGFR and ERK in murine prostate cancer cells

0.4×10^6 DVL3 cells were seeded in 6 well plate. When cells were confluent, they were washed two times with PBS. For the inhibition of EGFR phosphorylation, Erlotinib (Selleckchem, #S1023) was used at the following concentrations 1, 5 and 10 μM during 24 h in blank RPMI media. For inhibition of ERK phosphorylation, Trametinib (Selleckchem, #S2673) was used at the following concentrations 20 and 50 nM during 24 h in blank RPMI media. Inhibitions assay were stopped by washing the cells once with PBS and then harvested by scraping in RIPA buffer (Abcam, ab156034) with protease inhibitors (Roche, #05892970001) and phosphatase inhibitors (Roche, #04906845001), samples were incubated 10 min at 4C and disrupted mechanically. Subsequently, samples were centrifugated at 13,000 × rpm for 20 min at 4C, the supernatant were subjected to protein quantification, electrophoresis and immunoblotting.

Organotypic assay in DVL3 cancer cells

5,000 DVL3 cells were embedded in matrix BME (AMS Biotechnology (Europe) Limited, #3533-010-02) and cultivated in rGF media at 37°C, 5% CO_2 for 3 or 7 days respectively in organoid media with some modifications. The organoids were supplemented with or without 5α-Dihydrotestosterone (DHT) plus 100 ng/mL recombinant mouse AREG (R&D systems, # 989-AR-100), 50 ng/mL human EGF (Peprotech, #AF-100-15) or exclusion of any growth factor accordingly with the conditions desired to test.

Immunofluorescence of DVL3 organotypic cultures

Matrix embedded cells were fixed in 4% paraformaldehyde (Polysciences, #18814) for 1h at room temperature and then washed three times in PBS. Permeabilization was performed using the 2% Triton X-100 in PBS for 30 min. Primary antibodies were prepared in blocking buffer (2% Triton X-100, 2% FBS, 1% BSA in PBS) at the optimised concentrations and incubated over-night at 4C, followed by incubation with secondary antibodies. DAPI counterstaining was performed for 20 min. Confocal Ophera Phenix High Content Screening System (PerkinElmer) or Zeiss LSM880 was used for analysis.

Erlotinib and trametinib treatment in DVL3 cells plated in 3D conditions

DVL3 cells embedded in organoid matrix BME (AMS Biotechnology (Europe) Limited, #3533-010-02) were growth in rGF media with/without 5α-Dihydrotestosterone (DHT, 1nM) plus 100 ng/mL recombinant mouse AREG (R&D systems, # 989-AR-100) during 3 days. Then, organoids were washed with PBS and plated in the same media plus 20uM of Erlotinib (Selleckchem, #S1023), 100nM of Trametinib (Selleckchem, #S2673) or vehicle control (DMSO) for 4 days. At the end of the experiment, the DVL3 organoids were fixed in 4% paraformaldehyde (Polysciences, #18814) and imaged on the confocal Opera Phenix High Content Screening System (PerkinElmer) and EVOS microscope. Image analysis of the non-covered area by organoids were performed with Fiji software.

Protein quantification

Protein quantification was performed with the BCA Protein Assay Kit (Thermo Scientific, #23227) accordingly to manufacturers' instructions. After that, each sample was diluted into loading Buffer 4x (Bio-Rad, #1610747), heated to 95°C for 5 min.

Western blot

Samples were separated on a 4–20% TGX Precast Protein Gels (Bio-Rad, #4561095) following manufacturer's instructions. For immunodetection, gels were transferred onto a 0.2 μm PVDF Membrane (Bio-Rad, #1620177) by wet transfer. Non-specific binding sites were blocked by incubating membranes in blocking buffer at room temperature for 1h. The membranes were incubated overnight at 4°C in their respective conditions (Table S6), the membrane was washed three times with TBST or PBST and incubated with horseradish peroxidase (HRP)-linked antibodies in TBST or TBST supplemented with non-fat dry milk at room temperature for 1 h, followed by three additional washes. Signal was detected by chemiluminescence substrate (ThermoScientific, #32132) using the Bio-Rad Chemidoc Imagining System.

RNA extraction and cDNA synthesis

Total RNA from cultivated or organoids DVL3 cells was extracted using the RNeasy Plus Mini Kit (50) (Qiagen, #74134). Evaluation of RNA quality was performed NanoDrop ND-1000 (Thermo Scientific). First strand synthesis was performed starting from 0.5 μg of total RNA with the Script cDNA Synthesis Kit (Bio-Rad, #1708891). First strand cDNA was used in qRT-PCR reactions that were performed in triplicate using FastStart Essential DNA Green Master (Roche, #06402712001) in a Roche Lightcycler 96, according to the manufacturers' recommendations.

Immunohistochemical analysis

Paraffin-embedded tissue sections (4μm thick sections) were deparaffinized and rehydrated. Epitope retrieval was performed using Epitope Retrieval Solution 1 (ER1) for pH 6 or ER2 for pH 9 (Leica, #AR9961 and #AR9640, respectively). Endogenous peroxidase activity was quenched by 10min pre-treatment with 3% hydrogen peroxide. Casein blocking solution (Vector labs, #SP-5020) was used. All antibodies used are listed in the key resources table. Multiplex immunofluorescence was performed on the Leica Bond RX automated IHC platform. Primary and secondary antibodies were incubated for 30 min at RT. The Envision-HRP Mouse or Rabbit reagents were used for the detection of the primary antibodies (Agilent, #K406311-2). The detection was enabled by the tyramide signal amplification method using the Opal Automation IHC kit (Akoya, #NEL821001KT) with three reactive fluorophores (Opal 520, Opal 570 and Opal 670). Nuclei were stained with DAPI.

For the RNA detection by *in situ* hybridization (ISH) the deparaffinized and rehydrated slides were pre-treated with the Proteinase K for 15 min. The RNAscope 2.5 LS Probe - Mm-*Ly6d* (ACD, #532078) was used and either BaseScope Red or ACD Multiplex Fluorescent detection kit was used for the chromogenic or IF detection, respectively (ACD, 320850). The sections were then incubated with the K8 antibody (ab53280, 1/400), AREG antibody (DF6665, 1/5000) or phospho-ERK antibody (#9101, 1/400). The IF slides were counterstained with DAPI and mounted with ProLong Gold Antifade Mountant (ThermoFisher, #P10144).

For the TMA blocks and the pre-/post-ADT samples, 5 μm sections and the tissue was processed were prepared for the multiplex immunohistochemistry as described above. For the staining, the anti-human LY6D, PSMA and pan-Cytokeratin antibodies were used (listed in key resources table). Nuclei were stained with DAPI. All the multiplexed tissue assays were performed on the Leica Bond RX automated IHC platform. Digital slide scanning was performed with the Olympus VS.1200 system. StarDist deep-learning algorithm was used for the nuclear detection.

Slides were scanned using the Leica SCN400 Slide Scanner or the Olympus VS.200 system. Image analysis was performed using the Halo image analysis platform (Indica Labs) or the QuPath v0.2.3 software (Bankhead et al., 2017).

For cytopsin analysis, FACS-purified luminal cells were spined down on glass slides, then fixed in 4% formalin for 10 min. Primary and secondary antibodies were incubated for 30 min at RT, at the following concentrations: anti- AREG antibody (1:100), phosphor-ERK (1:100) and LY6D antibody (1:100). All antibodies used are listed in the key resources table. Nuclei were stained with DAPI. Samples were then imaged on Olympus Spinning Disk microscope (Olympus IXplore Spin SR10) and analyzed using the FiJI software.

Gene expression analysis

For RNA sequencing (RNA-seq), total RNA from FACS-purified luminal cells was isolated using an RNA/DNA Purification Micro Kit (Norgen, #50300). RNA in each sample was reverse transcribed and amplified into cDNA. A modified Smart-Seq2 protocol was used for the generation of full-length cDNA and sequencing libraries. Briefly, RNA Sequence library preparation was performed according to a modified Smartseq2 protocol (Picelli et al., 2014) using Superscript II (Thermo Fisher, #18064022) for reverse transcription of polyA-RNA and Kapa Hifi Hotstart Readymix PCR kit (Roche, #KR0370) for second strand synthesis and amplification. Tagmentation reactions were carried out using a Nextera XT DNA Library Preparation Kit (Illumina, #FC-131-1024). Libraries were quantified using Kapa Library Quantification Kit for Illumina Sequencing Platforms (Roche, #07960336001). Single read 75bp sequencing was carried out by clustering 2pM of pooled libraries on a Nextseq500 sequencer (Illumina). The quantity and quality of each sample was measured using an Agilent 2100 Bioanalyzer. bcl2fastq was used for converting BCL data to fastq format, coupled with adaptor trimming. Sequencing reads were then mapped to mouse genome (mm.9) using STAR. Differential gene expression (DGE) analysis of the RNAseq data was done using edgeR Bioconductor package.[83] Read counts were normalized and log2 transformed. The log2-fold-change was computed and a threshold of $-1 \geq \text{logFC} \geq 1$, FDR <0.05 was applied for the downstream pathway analysis, gene ontology and DGE visualization.

For real-time PCR (RT-PCR) analysis, total RNA from FACS-purified luminal cells was isolated using PureLink RNA MicroKit (Invitrogen, 12183-016). RNA in each sample was reverse transcribed into cDNA using the High-Capacity cDNA Reverse Transcription Kit

(Applied Biosystems, #4368814). SYBR Green PCR Master Mix (Applied Biosystems, #4309155) was used for qPCR reaction. Primers are listed in Table S5.

Gene silencing by small interference RNAs (siRNAs)

Prostate luminal cancer cells (DVL3) were transfected with 50 nM siRNA (siEgr1 and non-targeting control) from Dharmacon (Table S5) using DharmaFECT 3 solution (Dharmacon, #T-2003-01) according to the manufacturer instructions. Transfected cells were embedded in matrix BME (AMS Biotechnology (Europe) Limited, #3533-010-02) and cultivated in complete mPOM media at 37°C, 5% CO_2 for 7 days.

Data analysis and visualization

RNA-seq data visualization

Differentially expressed genes were visualized in R by the implementation of heatmaps using the *pheatmap* package, or volcano plots using the *EnhancedVolcano* package. 4-way scatterplot was created by the set of functions within the *ggplot2/tidyverse* package.

PCA

Principal Component Analysis (PCA) was performed using the *PCAtools* Bioconductor package (Blighe & Lun, 2019). Data was visualised with the *biplot* function. Log_2-transformed normalised counts of the K8PY RNAseq dataset were used for the analysis.

GSEA

The molecular pathways enrichment was evaluated with the Gene Set Enrichment Analysis (GSEA) software.[92,93] For the analysis, normalised counts of the K8Y and K8PY bulk RNAseq dataset was used. The Hallmark and Gene Ontology (GO) gene set collections were evaluated using the GSEA software.

Evaluation of PC3 and DU145 datasets were obtained from the study by Xu et al., GEO accession: GSE116864.[41] The RNA-seq datasets of the PC3 and DU145 cells treated with the AREG-conditioned media, and their controls were selected for the analysis. Analysis was made in R using the package *DESeq2* in order to identify differentially expressed genes. Data was normalised and extracted for highly differentially expressed genes according to the following threshold: padj_cutoff = 0.05 and LogFC_cutoff = 1.5. GSEA was run to evaluate these gene sets in the K8Y and K8PY RNA-seq data.

Additional growth factor associated pathways were assessed using the MSigDB canonical pathways of the curated gene sets (C2). For the analysis we used the gene set signatures from the BioCarta, KEGG and Reactome datasets (Table S7).

IPA

The Ingenuity Pathway Analysis (IPA, Qiagen) was used to identify the canonical pathways activated in YFP^+ $LY6D^+$ versus YFP^+ $LY6D^-$ prostate cells isolated from K8PY HN or K8PY CR mice. Differentially expressed genes were filtered based on the $-1 \geq$ logFC ≥ 1.

DoRothEA

The transcription factor (TF) activity was inferred from the K8PY gene expression data by the *DoRothEA* package.[39] Data visualization was done using the *pheatmap* package.

Correlation analysis

Spearman correlation analysis was performed on the K8Y and K8PY RNA-seq dataset in R using the packages *ggplot2* and *ggpubr* and function *ggscatter*. Heatmaps were created with the packages pheatmap package. Genesets used for this study: GSE116864,[41] GSE94574.[37]

QUANTIFICATION AND STATISTICAL ANALYSIS

All statistical analyses were performed using GraphPad Prism v9.0.0 or in the R environment v4.0.2 (R Core Team). Data points from the individual technical and biological replicates are represented on the plots together with the means ± s.d. The statistical significance was assessed by t test or ANOVA based on the number of compared groups, two, or >2 groups, respectively. The p value is represented on the plots and each comparison is annotated. The number of independent experiments or biologically replicates are indicated in figure legends.